

1 Application of Nosé-Hoover Dynamics for Coarse-Graining Molecular Systems: An 2 Evaluation of Reproducibility in Lennard-Jones Systems

3 Toru Yamada¹ and Yohei Morinishi¹

4 *Graduate School of Engineering, Nagoya Institute of Technology, Gokiso-cho, Showa-ku,*
5 *Nagoya, 466-8555 Japan*

6 (*Electronic mail: yamada.toru@nitech.ac.jp)

7 (Dated: 1 March 2025)

8 This study proposes an application of Nosé-Hoover (NH) dynamics as a coarse-graining
9 (CG) method for molecular simulations, offering an alternative to traditional Langevin-
10 based approaches. The NH dynamics, known for its deterministic temperature control
11 without stochastic forces, is adapted here to model a monoatomic Lennard-Jones systems
12 at different coarse-grained levels. The CG particle's equation of motion is derived from
13 atomic-level dynamics, linking NH thermostat terms with system properties obtained from
14 molecular dynamics (MD) simulations. Key parameters, including the thermostat coeffi-
15 cient and thermal inertia, are calibrated using the MD data to assess their impact on the
16 dynamic and structural reproducibility of the CG model. The calibration results suggest
17 the potential application of NH dynamics as a coarse-graining method. The effectiveness
18 of the proposed method is then evaluated through a set of CG simulations. The CG results
19 show stable energy regulation and promising accuracy in reproducing system properties,
20 particularly for mass diffusion, with opportunities for further refinement in representing
21 structural reproducibility and momentum diffusion.

22 **MANUSCRIPT SIGNIFICANCE**

23 This study proposes Nosé-Hoover (NH) dynamics as a novel coarse-graining (CG) method for
 24 molecular simulations, offering a deterministic alternative to Langevin-based approaches. The CG
 25 equations of motion are derived from atomic-level dynamics, with NH thermostat parameters cali-
 26 brated using molecular dynamics (MD) data. The method is applied to monoatomic Lennard-Jones
 27 systems, demonstrating stable energy regulation and accurate reproduction of system properties,
 28 particularly mass diffusion. While structural and momentum diffusion reproducibility require fur-
 29 ther refinement, the results establish NH dynamics as a promising framework for CG simulations,
 30 combining deterministic temperature control with high fidelity in dynamic and structural repre-
 31 sentation.

I. INTRODUCTION

In recent years, coarse-grained (CG) methods have become increasingly important in the field of molecular dynamics (MD) simulations for efficiently understanding the behavior of complex systems. The CG method is a widely used approach to reduce computational complexity while preserving the key structural and dynamic properties of the system by representing multiple atoms or molecules as single CG units. Traditionally, models based on the Langevin equation have been widely employed in such CG approaches¹ due to their ability to represent thermal fluctuations or Brownian motion through the inclusion of friction and random forces. Various CG methods using Langevin dynamics have been developed, including dissipative particle dynamics (DPD)^{2,3}, Brownian dynamics (BD)⁴, and coarse-grained molecular dynamics (CGMD)⁵. Each method aims to reproduce specific physical properties, facilitating a wide range of applications such as simulations of biomolecular systems, polymer solutions, interfacial phenomena, and complex fluids^{6,7}. The adoption of these CG approaches has enabled the modeling of phenomena on the mesoscale, which is generally described as spanning spatial dimensions from 10 to 10⁴ nanometers and temporal ranges from 1 to 10⁶ nanoseconds⁶, while significantly reducing computational costs. Consequently, these methods allow for efficient analysis of system behavior over broader temporal and spatial scales.

The Langevin dynamics is a type of thermostat method, commonly used to regulate temperature in MD simulations. Over the years, various thermostat methods have been developed, which can be broadly categorized into stochastic and deterministic approaches¹. Stochastic methods^{8–10}, like Langevin dynamics, introduce random forces to represent thermal fluctuations. In contrast, deterministic methods^{11–15} control temperature through systematic adjustments without the inclusion of random forces. An equation of motion involving stochastic thermostat can be interpreted as describing the dynamics of a system that has undergone some form of coarse-graining; hence, it is conceivable that coarse-graining can also be achieved using deterministic methods. To the best of the authors' knowledge, however, no studies have yet applied deterministic thermostats in CG methods. This study specifically focuses on the Nosé-Hoover (NH) method, a well-known deterministic thermostat in molecular dynamics, and explores its application within CG modeling.

The NH method¹³, a widely used method in MD simulations, was developed as an efficient approach to maintain constant temperature during simulations. This technique provides a deterministic means of temperature control by coupling the system to a thermal reservoir through additional

degrees of freedom. Unlike stochastic thermostats, which rely on random forces to mimic thermal fluctuations, the NH thermostat achieves temperature regulation by dynamically adjusting the velocities of particles in response to deviations from the desired temperature. This allows for smooth energy exchange between the system and the thermal bath, ensuring more accurate reproduction of equilibrium properties. Over time, the NH method has been further developed, including the introduction of Nosé-Hoover Chains (NHC)¹⁴, which improve stability and enable effective temperature control in complex systems, and Galilean-invariant NH methods^{16–18}, which satisfies the Galilean invariance and linear and angular momentum conservations. Given these characteristics, NH-type methods may also have the potential to be applied in CG methods.

CG methods are, as described earlier, frequently employed to model liquids with high Schmidt numbers (Sc). Therefore, it is essential for these methods to accurately capture the high viscosity and slow diffusion characteristics of such systems. However, both the NH and Langevin methods face challenges in achieving this, as they are primarily optimized for short-timescale control, which limits their ability to represent the dynamics of high-Sc systems⁹. In the cases of DPD studies, for example, previous studies have highlighted the challenges of achieving realistic Schmidt numbers in DPD-based coarse-graining^{19–28}. Kumar et al.¹⁹ demonstrated that the Sc value in the CG water system significantly deviated from the value of water with increasing the level of coarse-graining while $Sc \approx O(10^3)$ was attained for lower CG levels. Similarly, Li et al.²⁰ applied an energy-conserving DPD approach and successfully reproduced the temperature dependence of water's dynamic properties while the CG level of the system was unclear due to their top-down parameterization method. In contrast, Lei et al.²¹ adopted a bottom-up DPD approach and achieved the Sc values ranging from 10 to 100, with accuracy comparable to their MD simulations. Furthermore, Liu et al.²² provided a comprehensive review of DPD studies, presenting parameter-based formulations for tuning the Sc value to match real fluids.

Conversely to the extensive studies on CG methods using Langevin dynamics, to the best of the authors' knowledge, there have been no studies applying Nosé-Hoover dynamics or other deterministic thermostats to CG methods while evaluating dynamic properties. Nevertheless, the NH dynamics offers several potential advantages over the Langevin thermostat. First, the NH method can provide smoother energy control through deterministic temperature regulation due to absence of the stochastic term. This has the potential to address the statistical error and intrinsically low temporal accuracy in stochastic methods²⁹ while modifying time marching methods can reduce these errors due to the stochastic term^{30,31}. The NH method also avoids the noise introduced by

random forces in Langevin dynamics, thereby allowing more precise energy maintenance, especially in equilibrium states. Furthermore, NH-based methods can be extended for application to high-Sc systems by incorporating recent developments in Langevin dynamics. Given these advantages, it is important to first investigate whether coarse-graining with the NH thermostat is feasible.

In this study, the NH dynamics is applied to coarse-graining for the first time, with the aim of evaluating the reproducibility of the proposed CG method. Specifically, a monoatomic Lennard-Jones (LJ) system is considered, and the equation of motion for coarse-grained particles is derived from the atomic-level equations of motion. Next, terms in the coarse-grained equation that cannot be directly represented are associated with the NH thermostat terms, and the thermostat coefficient is obtained using MD simulations to examine its temporal characteristics. Finally, CG simulations are conducted to evaluate the reproducibility of the dynamic and structural properties of the CG system by comparing these with available studies of Langevin dynamics, as well as the thermostat coefficient, and the effectiveness of the proposed method is discussed.

This paper proceeds as follows: In Section II, we describe the methodology of applying the NH dynamics to the CG model, including the derivation of the equations of motion and the introduction of the Galilean-invariant thermostat. Section III presents the MD simulations, detailing the setup, parameters, and results for the reference CG systems. Section IV discusses the results of the CG simulations, comparing them with the MD results to evaluate the performance of the proposed model. Finally, Section V concludes the study, summarizing the findings and outlining potential directions for future research.

II. METHODOLOGY

A. Deriving the equation of motion for a coarse-grained system

In this section, the overview of the method for coarse-graining atoms/molecules proposed in this study is described. It should be noted that this study focuses on monoatomic molecular systems governed only by the LJ potential for simplicity. The LJ potential is denoted by $U(\mathbf{q})$ where \mathbf{q} represents the position of atoms, and the equation of motion (EOM) for atoms is expressed as follows.

$$\frac{d\mathbf{p}_i}{dt} = -\frac{\partial U(\mathbf{q})}{\partial \mathbf{q}_i}. \quad (1)$$

In the above equation, \mathbf{p} is the momentum of the atom, i is the atom index ($i = 1, 2, \dots, N_{\text{atom}}$.
 N_{atom} : the total number of atoms in the computational domain). Similar to the existing studies^{21,23,24},
a CG particle assumes to be formed with n_{cg} atoms based on the following equations:

$$\mathbf{R}_{\eta} = \sum_k^{n_{\text{cg}}} \mathbf{q}_{(\eta, k)} / n_{\text{cg}}, \quad (2)$$

$$\mathbf{P}_{\eta} = \sum_k^{n_{\text{cg}}} \mathbf{p}_{(\eta, k)}, \quad (3)$$

where \mathbf{R} and \mathbf{P} are the position and momentum of the CG particle, respectively. The indices η
and k are the index of the CG particle and that of the atom within the belonging CG particle,
respectively. Hereafter, the atom index i is used for the atomic system, and (η, k) for the CG
system. Based on the Eqs.(1) and (3), the EOM for the CG particle can be described as follows.

$$\frac{d\mathbf{P}_{\eta}}{dt} = \sum_k^{n_{\text{cg}}} \frac{d\mathbf{p}_{(\eta, k)}}{dt} = \sum_k^{n_{\text{cg}}} \left[-\frac{\partial U(\mathbf{q})}{\partial \mathbf{q}_{(\eta, k)}} \right]. \quad (4)$$

Introducing a potential $\bar{U}(\mathbf{R})$ that depends only on the inter-CG-particle distance, Eq.(4) can be
rewritten as follows.

$$\frac{d\mathbf{P}_{\eta}}{dt} = -\frac{\partial \bar{U}(\mathbf{R})}{\partial \mathbf{R}_{\eta}} + \left\{ \left(\sum_k^{n_{\text{cg}}} \left[-\frac{\partial U(\mathbf{q})}{\partial \mathbf{q}_{(\eta, k)}} \right] \right) - \left[-\frac{\partial \bar{U}(\mathbf{R})}{\partial \mathbf{R}_{\eta}} \right] \right\}. \quad (5)$$

The first term inside the braces $\{ \}$ can be obtained from the atomic system. Therefore, in the CG
simulations, the part surrounded by the braces needs to be replaced with a term that appropriately
reproduce the behavior of CG particles. In this study, a NH type thermostat is applied as described
in the followings.

B. Galilean-invariant Nosé-Hoover thermostat

The NH thermostat¹³ is a well-known temperature control method used in MD simulations.
It is designed to enable the simulation of dynamic behaviors while maintaining a constant tem-
perature within the system. Specifically, the kinetic energy of a system is exchanged with that
of the thermostat to maintain the temperature of the system constant by introducing an additional
thermostat term in the EOM.

The original NH thermostat¹³, however, is not Galilean invariant, which is not adequate when
fluid-dynamic behaviors is taken into account in the system. For the sake of this invariance satisfied

for the EOM as with existing CG methods, e.g., DPD^{2,3}, a Galilean-invariant NH type (GINH) thermostat¹⁷, is used as the EOM for the CG system in this study, which is expressed as follows.

$$\frac{d\mathbf{P}_\eta}{dt} = -\frac{\partial \bar{U}(\mathbf{R})}{\partial \mathbf{R}_\eta} - \xi \mathcal{V}_\eta. \quad (6)$$

The above equation is referred to as "pairwise Nosé-Hoover thermostat"¹⁷ and is a direct deterministic counterpart to Galilean-invariant type Langevin thermostats (e.g., DPD). ξ in this equation is a variable thermostat coefficient regulating temperature of the system. \mathcal{V}_η represents a quantity calculated based on the relative velocity between CG particles, which is expressed as,

$$\mathcal{V}_\eta = \sum_{\theta \neq \eta} \mathcal{V}_{\eta\theta}, \quad (7)$$

$$\mathcal{V}_{\eta\theta} = W(R_{\eta\theta}) \left(\mathbf{V}_{\eta\theta} \cdot \hat{\mathbf{R}}_{\eta\theta} \right) \hat{\mathbf{R}}_{\eta\theta}, \quad (8)$$

where $W(R_{\eta\theta})$ is a weighting function, $\mathbf{V}_{\eta\theta} = \mathbf{V}_\eta - \mathbf{V}_\theta = \mathbf{P}_\eta/M_\eta - \mathbf{P}_\theta/M_\theta$ (M_η : mass of the η th CG particle), and $\hat{\mathbf{R}}_{\eta\theta} = \mathbf{R}_{\eta\theta}/R_{\eta\theta}$ ($R_{\eta\theta}$: Radial distance between η th and θ th CG particles). In this study, the following weighting function, which is the same as the previous study¹⁷, is used,

$$W(R) = \begin{cases} (1 - R/R_c)^2, & (R \leq R_c), \\ 0, & (R > R_c), \end{cases} \quad (9)$$

where R_c is the cutoff radius. The time evolution of the ξ value in Eq.(6) is described based on the following equation¹⁷:

$$\frac{d\xi}{dt} = Q_\xi^{-1} \sum_\eta \sum_{\theta > \eta} \left\{ W(R_{\eta\theta}) \left[\left(\mathbf{V}_{\eta\theta} \cdot \hat{\mathbf{R}}_{\eta\theta} \right)^2 - k_B T / \bar{M}_{\eta\theta} \right] \right\}. \quad (10)$$

Q_ξ in the above equation is a constant, called thermal inertia. This value controls the rate of energy flow between the system and thermostat, and as will be described in the later sections, this value governs the tendency of the fluctuation characteristics of ξ . Also, $\bar{M}_{\eta\theta}$ is the value based on the masses of η th and θ th CG particles by using $\bar{M}_{\eta\theta} = M_\eta M_\theta / (M_\eta + M_\theta)$.

C. Link between thermostat coefficient and atomic/CG quantities

The primary goal of this study is to reproduce the CG system generated by the MD simulation through the corresponding CG simulation by modeling Eq.(4) with Eq.(6). By equating these equations, the link between the thermostating coefficient, ξ , and the atomic/CG quantities can be

obtained as follows:

$$-\xi \mathcal{V}_\eta = \left\{ \sum_k^{n_{cg}} \left[-\frac{\partial U(\mathbf{q})}{\partial \mathbf{q}_{(\eta,k)}} \right] - \left[-\frac{\partial \bar{U}(\mathbf{R})}{\partial \mathbf{R}_\eta} \right] \right\}. \quad (11)$$

Multiplying both sides of the above equation by \mathcal{V}_η , ξ for each time step can be obtained with the quantities of the reference system as follows:

$$\begin{aligned} -\xi \mathcal{V}_\eta \cdot \mathcal{V}_\eta &= \left\{ \sum_k^{n_{cg}} \left[-\frac{\partial U(\mathbf{q})}{\partial \mathbf{q}_{(\eta,k)}} \right] - \left[-\frac{\partial \bar{U}(\mathbf{R})}{\partial \mathbf{R}_\eta} \right] \right\} \cdot \mathcal{V}_\eta, \\ \xi &= -\frac{\left\{ \sum_k^{n_{cg}} \left[-\frac{\partial U(\mathbf{q})}{\partial \mathbf{q}_{(\eta,k)}} \right] - \left[-\frac{\partial \bar{U}(\mathbf{R})}{\partial \mathbf{R}_\eta} \right] \right\} \cdot \mathcal{V}_\eta}{\mathcal{V}_\eta \cdot \mathcal{V}_\eta}. \end{aligned} \quad (12)$$

Based on the above equation, the same number of ξ values as the number of CG particles can be calculated for each computational step from an MD simulation while only one ξ value is used in CG simulations as shown in Eq.(6). Therefore, in this study, the averaged value, $\langle \xi \rangle$, is used to investigate the thermostat characteristics.

III. MD SIMULATION

A. Simulation details

In this study, a set of MD simulations are conducted to investigate the characteristics of the thermostat coefficient for the CG systems coarse-grained by the LJ monoatomic atoms. In line with most previous studies^{21,24}, the LJ atoms are constrained by the RATTLE^{24,32} method in order to form CG particles under the following condition.

$$\frac{1}{n_{cg}} \sum_k^{n_{cg}} (\mathbf{q}_{(\mu,k)} - \mathbf{R}_\mu)^2 = R_g, \quad (13)$$

where R_g is the constant radius of gyration depending on the degree of coarse-graining. R_g is selected such that the local number density of atoms within a CG particle corresponds to that for the system. In the RATTLE method, the constraint equations are solved using the Lagrange multiplier method, and both positions and velocities are iteratively corrected at each simulation time step to satisfy the constraint condition, ensuring that the relative distances between atoms within each CG particle remain fixed at R_g ³². The interatomic interactions are based only on the LJ (12-6) potential which is described as

$$U(q) = 4\epsilon \left[\left(\frac{\sigma}{q} \right)^{12} - \left(\frac{\sigma}{q} \right)^6 \right], \quad (14)$$

where q and (σ, ϵ) are the interatomic distance and LJ parameters, respectively. These parameters for argon atoms are used in this study.

Table I shows the simulation conditions for the MD simulations. The parameters are normalized with the LJ parameters listed at the top row of the table. There are three reference CG systems with different CG degrees, i.e., $n_{cg} = 4, 8$, and 12 (n_{cg} : Number of atoms consisting of a CG particle). The domains for all the systems are set to be a cubic surrounded by periodic boundaries for all the directions. All the MD simulations are initially performed using rescaling thermostat³³ with time steps much smaller than the value of Δt listed in Table I. Then, the systems are equilibrated in the microcanonical ensemble, i.e., without thermostat, with $\Delta t/t_{atom} = 1.0 \times 10^{-4}$, up to $t/t_{atom} = 100$ (t_{atom} : Normalization factor for time, see Appendix A). Finally, the data in an equilibrium state for postprocessing are acquired for $t/t_{atom} \geq 100$. The time marching method used are the velocity-Verlet method³⁴.

All the MD simulations are conducted by Molly.jl³⁵, a open source Julia code package for molecular simulations, with modifications to include the RATTLE constraint method³².

All the results in the subsequent sections are shown with normalized values, where normalization factors based on the values in the atomic system are listed in Appendix A.

B. CG characteristics obtained from the MD system

Three MD simulations are first performed to evaluate the characteristics of the CG systems with different CG degrees. Figure 1 shows the temperature histories of the atomic and CG systems obtained from the simulations for $n_{cg} = 4, 8$, and 12 , where the temperatures of these systems are calculated with the kinetic energy of atoms and CG particles, respectively, i.e., $k_B T_{atom} = \frac{1}{3} \langle \mathbf{p} \cdot \mathbf{p} / m \rangle$ for the atomic system and $k_B T_{cg} = \frac{1}{3} \langle \mathbf{P} \cdot \mathbf{P} / M \rangle$ for the CG system. It can be seen from the figures that the temperature of the CG systems are slightly higher up to 10% than those in the atomic systems regardless of n_{cg} . This can be attributed to the definition of the momenta of CG particles resulting in extra contributions to the CG temperature, that is,

$$\begin{aligned} \mathbf{P}_\eta \cdot \mathbf{P}_\eta &= \left(\sum_k^{n_{cg}} \mathbf{p}_{(\eta, k)} \right) \cdot \left(\sum_k^{n_{cg}} \mathbf{p}_{(\eta, k)} \right) \\ &= \sum_k^{n_{cg}} \mathbf{p}_{(\eta, k)} \cdot \mathbf{p}_{(\eta, k)} + \sum_r \left(\sum_k^{n_{cg}} \right) \mathbf{p}_{(\eta, r)} \cdot \mathbf{p}_{(\eta, r)} \end{aligned} \quad (15)$$

To further examine the characteristics of the CG systems, we analyze the probability density

TABLE I. Computational conditions for the MD simulations. All the parameters are dimensionless except for the LJ parameters.

Parameter	Value
LJ parameters (σ_{atom} [nm], ϵ_{atom} [kJ/mol], m_{atom} [u])	(0.34, 0.998, 39.95)
Computational domain	Cube (Cartesian coordinate system)
Boundary conditions	Periodic for all the directions
Total number of atoms, N_{atom}	13500, 27000, 40500
Side length of domain, l/σ_{atom}	26.80, 33.76, 38.56
Cutoff radius for interatomic interaction	$0.5l$
Number density of atoms, ρ_{atom}	0.701
Coarse-graining degree, n_{cg}	4, 8, 12
Number of CG particles in the system, N_{cg}	3375
Constant radius of gyration, R_g/σ_{atom}	1.109, 1.397, 1.597
Number density of CG particles, ρ_{cg}	0.175, 0.0876, 0.0584
System temperature, $k_B T/\epsilon_{\text{atom}}$	1.0
Time increment, $\Delta t/t_{\text{atom}}$	1.0×10^{-4}
Constraint method	RATTLE ³²

227 function (PDF) of the speed obtained from the MD simulations. Figure 2 presents the speed
 228 distributions for the atomic and CG systems with $n_{\text{cg}} = 4, 8$, and 12, where the circles indicate
 229 the computed values and the solid lines represent the theoretical Maxwell-Boltzmann distribution.
 230 The results show that both the atomic and CG systems exhibit good agreement with the theoretical
 231 distribution, confirming that the velocity distributions follow the expected equilibrium behavior.

232 Turning into structural characteristics, Figure 3 provides the radial distribution functions, $g(r)$,
 233 for the atoms and CG particles obtained from the MD simulations with different n_{cg} degrees. In
 234 this figure, r_{atom} represents the general interparticle distance between individual atoms, distinct
 235 from q in Eq. (14), which denotes the radial distance between atomic pairs in $g(r)$ and force
 236 distributions shown in the later sections. Similarly, r_{cg} represents the general interparticle distance
 237 between CG particles, playing the same role at the CG scale as r_{atom} does for the atoms. First,
 238 it is explicitly revealed in Figure 3(a) that $g(r)$ of the atoms is not affected by the n_{cg} number
 239 despite the constraint conditions. This suggests that the influence of the RATTLE constraints on

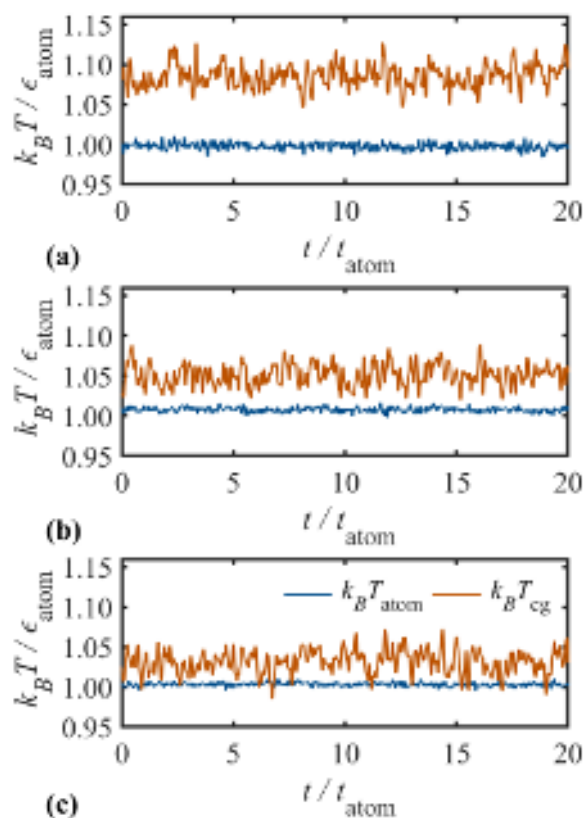


FIG. 1. Temperature histories of the atomic and CG systems, $k_B T_{\text{atom}}$ (blue line) and $k_B T_{\text{cg}}$ (orange line), respectively, obtained from the MD simulations for (a) $n_{\text{cg}} = 4$, (b) $n_{\text{cg}} = 8$, and (c) $n_{\text{cg}} = 12$. The values are normalized by the atomic LJ parameters.

the structural characteristics of the atomic system is negligible.

On the other hand, as can be seen in Figure 3(b), the $g(r)$ for CG particles differ depending on n_{cg} . This difference arises because the value of R_g used in the constraint conditions varies with n_{cg} , leading to changes in the effective structure of the CG system. Therefore, while the atomic system remains unchanged, the RATTLE constraints play a role in determining the structural characteristics of the CG system.

Similar to the radial distribution function, the spatial distribution of the number density of CG particles is important for gaining insights into macroscopic structure of the CG system. Figure 4 shows the distribution of the number density, ρ , in the x -direction obtained from the MD sim-

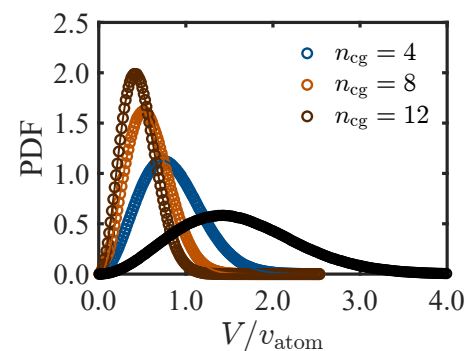


FIG. 2. Probability density function (PDF) of the speed for the atomic and CG systems obtained from MD simulations for for $n_{\text{cg}} = 4$ (blue), $n_{\text{cg}} = 8$ (orange), and $n_{\text{cg}} = 12$ (dark orange). The black color indicates the result of the atomic system for $n_{\text{cg}} = 4$ as a reference.

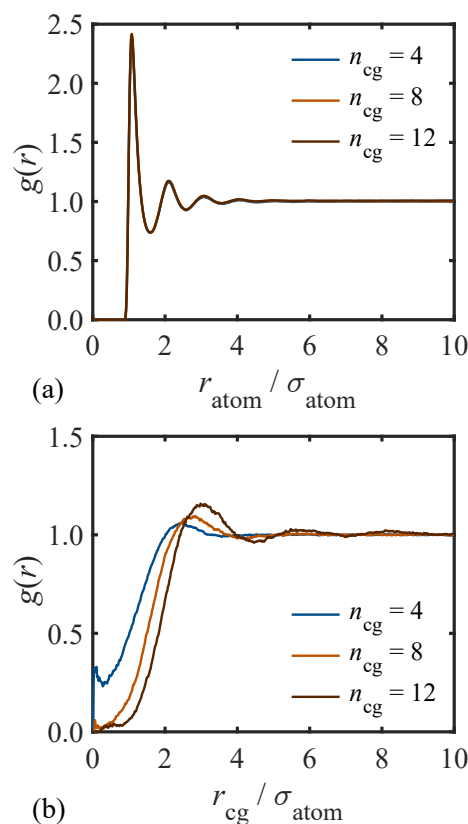


FIG. 3. Radial distribution function, $g(r)$, of (a) the atoms and (b) the CG particles obtained from the MD simulations for $n_{\text{cg}} = 4$ (blue), $n_{\text{cg}} = 8$ (orange), and $n_{\text{cg}} = 12$ (dark orange).

ulations for different CG degrees, where the distribution of atoms for $n_{\text{cg}} = 8$ is also shown as a reference. As can be seen from the figure, the distribution of CG particles exhibits greater spatial fluctuation compared to the distribution of atoms. Furthermore, it is observed that these fluctuations become more regular and larger as the n_{cg} value increases. This phenomenon is presumed to be because the CG particles are not mass points but have a certain size of R_g . As the size increases, the system becomes more structured, where the range of particle movement is limited. Indeed, in the case of $n_{\text{cg}} = 12$, there are fifteen clear positive peaks observed. This corresponds to the number of CG particles per direction in the case that the particles are uniformly aligned in the computational domain (that is, the cube root of 3375 is 15).

Figure 5 presents the distributions of the average inter-CG-particle potential forces, $\langle F(r) \rangle$, calculated from the MD simulations for $n_{\text{cg}} = 4, 8$, and 12, where $\langle F(r) \rangle$ is calculated with $\langle F(r) \rangle = \langle \mathbf{F}_{\eta\theta} \cdot \hat{\mathbf{R}}_{\eta\theta} \rangle$ ($\mathbf{F}_{\eta\theta}$: Instantaneous force acting on η th CG particle from θ th one^{21,23,24}). As is shown in this figure, for all the cases, the distributions are much softer than that of LJ poten-

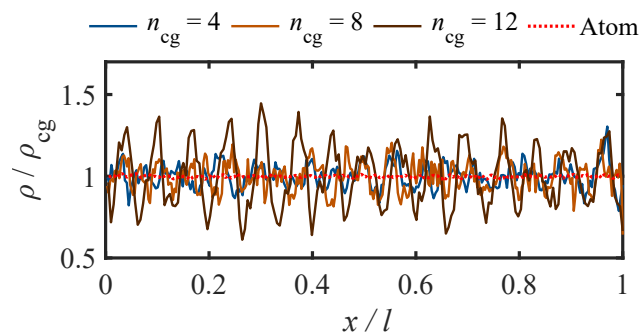


FIG. 4. Number density distribution of the CG particles obtained from the MD simulations for $n_{cg} = 4$ (blue), $n_{cg} = 8$ (orange), and $n_{cg} = 12$ (dark orange). The distribution of atoms for the case of $n_{cg} = 8$ is also shown with red dotted line as a reference.

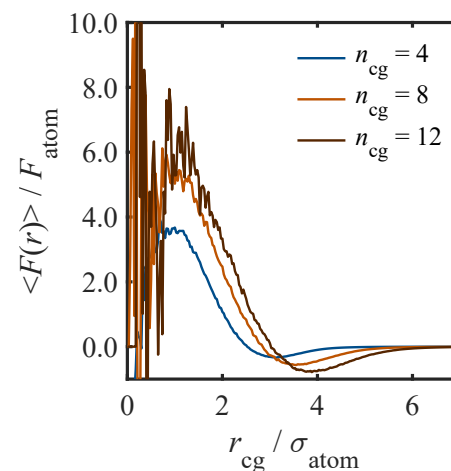


FIG. 5. Inter-CG-particle force distributions for different n_{cg} cases.

263 tial. This is attributed to vanishing of many-body effects due to coarse-graining. The many-body
264 interactions between atoms observed in the atomic system are averaged into simpler interactions
265 between the centers of mass of CG particles in the CG system. This figure also reveals that the
266 locations of peak and well shift away from the CG particle center as n_{cg} becomes larger. This is
267 reasonable because the radius of CG particle, R_g , increases with n_{cg} becoming larger. It should be
268 worth noting that the large fluctuations in the vicinity of the particle center is due to insufficient
269 CG particle pairs for ensemble average. This will not pose a problem because this part is used nei-
270 ther for calculating the thermostat coefficient, ξ , or for the potential force in the CG simulations
271 as described in the later sections.

272 C. Estimation of GINH coefficients

273 *Parameter setting in Eq.(12)*

274 As described in Sec.II C, the governing equations of the atomic and CG systems can be linked
275 with the thermostat coefficient, ξ , through Eq.(12), and thus understanding ξ 's dynamic character-
276 istics is essential for better CG modeling.

277 Modeling of the inter-CG-particle potential, \bar{U} , holds significant importance as it determines
278 the structural and dynamic characteristics of CG systems in this study. Existing CG methods

employing Langevin type thermostats, such as DPD², include a stochastic term. This term makes a significant contribution especially to the dynamic characteristics, such as the diffusion coefficient and shear viscosity, more than the potential force term. Whereas the NH type thermostat, utilized in the present study, does not include the stochastic term. Consequently, CG simulations can easily diverge if the soft potential-derived forces (see Figure 5) are used. In addition, the inter-CG-particle potential force, $-\partial\bar{U}/\partial\mathbf{R}_\eta$, exclusively determines both the structural and dynamic characteristics. Therefore, in this study, the LJ potential (Eq.(14)) is applied to model \bar{U} , and the reproducibility of the CG system, especially dynamic characteristics, using such a simple approximation of the potential force along with the NH thermostat will be evaluated.

The LJ parameters for \bar{U} are estimated as follows: For the effective diameter, σ , it is assumed to be related to the side length of a cube corresponding to the volume occupied by a single atom or CG particle. This can be expressed as,

$$L_{\text{sys}} = \left(\frac{V}{N_{\text{sys}}} \right)^{1/3}, \quad (16)$$

where V is the total system volume, and subscript "sys" denotes either "atom" or "cg" indicating the length for the atom or CG particle. Assuming that the proportion of these scales corresponds to the diameters of the atomic and CG systems, i.e.,

$$\frac{L_{\text{atom}}}{\sigma_{\text{atom}}} = \frac{L_{\text{cg}}}{\sigma_{\text{cg}}},$$

the effective diameter for the inter-CG potential is expressed as the following equation:

$$\sigma_{\text{cg}} = \sigma_{\text{atom}} \times \frac{L_{\text{cg}}}{L_{\text{atom}}}.$$

Substituting Eq.(16) and $N_{\text{atom}} = n_{\text{cg}} N_{\text{cg}}$ in to the above equation, one can obtain,

$$\sigma_{\text{cg}} = \sigma_{\text{atom}} \times n_{\text{cg}}^{1/3}. \quad (17)$$

The potential well, ϵ determines the kinetic temperature in CG simulations, and thus it is chosen as the average kinetic temperature of CG systems calculated from the MD simulations. The calculated values of σ and ϵ of the CG systems, σ_{cg} and ϵ_{cg} , for different n_{cg} are summarized in Table II.

Figure 6 presents a comparison between the average inter-CG-particle force, $\langle F(r) \rangle$, calculated from the MD simulation at a CG degree of $n_{\text{cg}} = 8$ and the LJ force profile (the model function for $-\partial\bar{U}/\partial\mathbf{R}_\eta$ in the CG simulation) with $(\sigma_{\text{cg}}/\sigma_{\text{atom}}, \epsilon_{\text{cg}}/\epsilon_{\text{atom}}) = (2.0, 1.051)$ for $n_{\text{cg}} = 8$ as listed

TABLE II. σ_{cg} and ϵ_{cg} for different n_{cg} .

n_{cg}	4	8	12
$\sigma_{cg}/\sigma_{atom}$	1.588	2.000	2.289
$\epsilon_{cg}/\epsilon_{atom}$	1.083	1.051	1.032

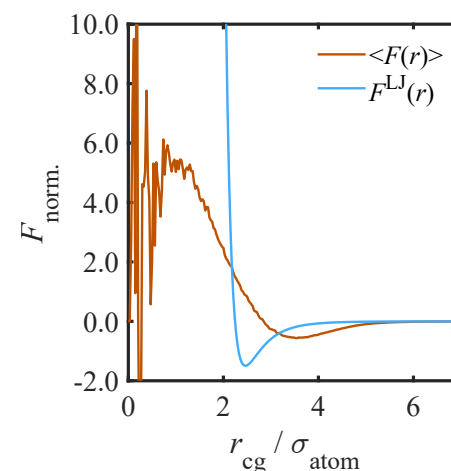


FIG. 6. Calculated and modeled inter-CG-particle force distributions, $F(r)$ and $F^{LJ}(r)$, for $n_{cg} = 8$ ($F_{norm.}$ in the vertical axis is the normalized value of either $F(r)$ or $F^{LJ}(r)$).

in Table II. As illustrated in the figure, the two distributions hardly coincide, and the difference between them for $r/\sigma_{cg} < 2$ is nearly infinite due to the characteristics of the LJ potential force. Therefore, to avoid including the infinite difference in the calculation of ΔF in Eq.(12), the differences for $r/\sigma_{cg} < 2^{1/6}$ ($r/\sigma_{cg} = 2^{1/6}$ is the interparticle distance at which the model's potential force becomes zero) are not considered.

The final parameter required for calculating ξ based on the results of the MD simulations using Eq.(12) is the cutoff radius R_c for the weighting function in Eq.(9). Taking another look at Figure 3(b), it can be seen that the influence of the CG interparticle potential diminishes beyond approximately $r/\sigma_{atom} > 7$. With this in consideration, the cutoff radius is set as $R_c/\sigma_{atom} = 7$ to estimate the values of ξ . The same value is used for the inter-CG-particle potential force in the CG simulations.

ξ characteristics

Figures 7 and 8 show the history of $\langle \xi \rangle$ and the profile of power density, P_ξ , for the atomic systems with different CG degrees, where $\langle \xi \rangle$ represents the coefficient averaged over the CG particles during each time step. Figure 7 reveals that the value of $\langle \xi \rangle$ exhibits fluctuations centered around zero, regardless of the size of n_{cg} , and the pattern of these fluctuations appears to be similar.

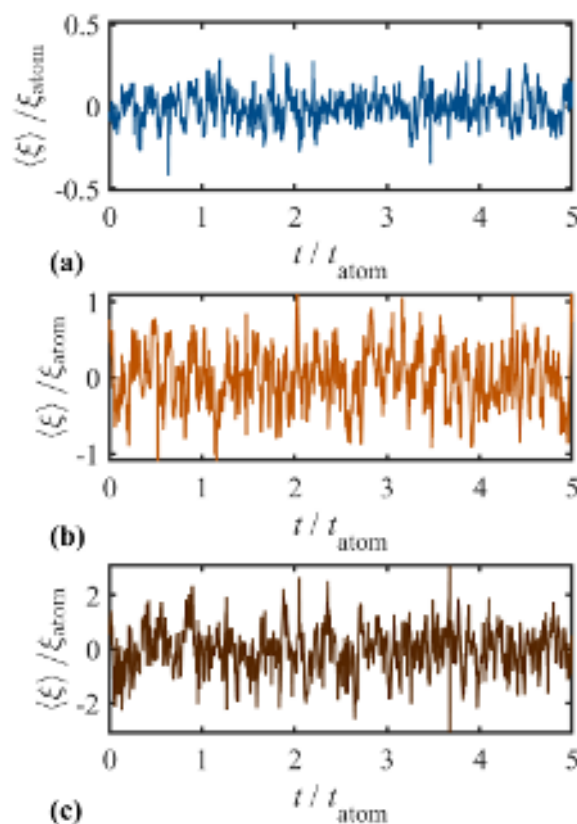


FIG. 7. Averaged thermostat coefficient history, $\langle \xi \rangle$, calculated with Eq.(12) from the atomic system for (a) $n_{cg} = 4$, (b) $n_{cg} = 8$, and (c) $n_{cg} = 12$.

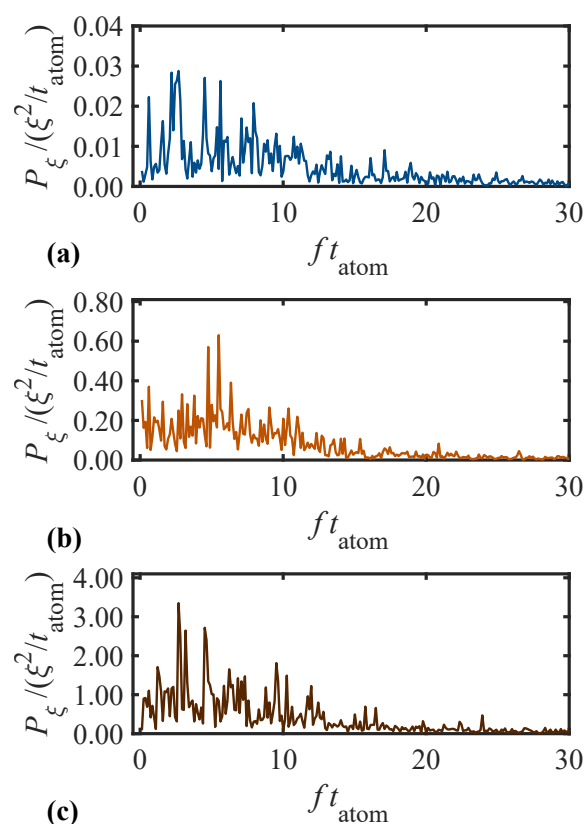


FIG. 8. Spectral characteristics of power density of $\langle \xi \rangle$ for (a) $n_{cg} = 4$, (b) $n_{cg} = 8$, and (c) $n_{cg} = 12$.

324 Additionally, it is discernible that the amplitude of $\langle \xi \rangle$ escalates as n_{cg} increases. The observation
325 that the calculated $\langle \xi \rangle$ demonstrates fluctuations centered around zero is favorably received. This
326 is because, within the context of the NH type thermostat, a similar temperature control behavior
327 is exhibited although the fluctuation demonstrates more harmonic oscillator-like behavior. This
328 suggests that the NH type thermostat can be a potential application as the governing equation for
329 CG particles. From the power spectral density of $\langle \xi \rangle$ of Figure 8, it is confirmed that $\langle \xi \rangle$ possesses
330 a band spectrum for frequencies $ft_{atom} < 10$. Moreover, P_{ξ} reveals multiple peaks approximately
331 within the frequency region of $2 < ft_{atom} < 7$ where the number depends on the CG degree. These
332 fluctuation characteristics can be interpreted as those of the "spring" connected between the system
333 and the GINH thermostat. This characteristics is directly related to the thermal inertia, Q_{ξ} , and it
334 is considered, by appropriately choosing this value, that the fluctuation characteristics of $\langle \xi \rangle$ can
335 be accurately replicated.

TABLE III. Thermal inertia, Q_ξ , derived from the MD simulations using LSM. Q_ξ^* : Normalized Q_ξ ($Q_\xi^* = Q_\xi / Q_{\xi, \text{atom}}$).

n_{cg}	4	8	12
Q_ξ^*	54.84	805.0	3242

In this study, the thermal inertia, Q_ξ , was initially derived using the least squares method (LSM) based on the time evolution of $\langle \xi \rangle$, the details for which is described in Appendix B. Table III shows the Q_ξ values derived from the MD simulations with different n_{cg} using the LSM. Based on this table, it is evident that there is a tendency for the Q_ξ value to increase with larger value of n_{cg} . However, since ξ is determined for each particle in MD simulations but is a single system-wide value in CG simulations, its fluctuation characteristics may differ. The values of $\langle \xi \rangle$ derived from the MD simulations contain broader frequency components than the ξ in the CG simulations, which affects the accuracy of Q_ξ . This discrepancy explains why the least squares method did not yield a Q_ξ value that correctly reproduces the fluctuation characteristics of ξ in CG simulations. This issue will be further analyzed in Appendix D, where we discuss the relationship between Q_ξ and ξ 's frequency characteristics.

IV. CG SIMULATION

A. Simulation details

The CG simulations are performed by using the parameters based on the MD simulations described in the previous sections. Table IV shows the simulation conditions for the CG simulations. There are three CG systems with the different CG degrees, i.e., $n_{\text{cg}} = 4, 8$, and 12 . The domains for all the systems are set to be a cubic surrounded by periodic boundaries for all the directions as was set for the MD simulations. The time increment, Δt , is ten times greater than that used for the MD simulations. Concerning the time increment, in conventional MD simulations of LJ systems, $\Delta t / t_{\text{atom}} \approx 10^{-3}$ is typically used^{26,28,36}. However, in the present MD simulations, a smaller value was used due to the application of the RATTLE³² constraints, to ensure the temporal resolution of particle motion (see Table I). In the CG simulations, however, the time increment was set to $\Delta t / t_{\text{atom}} = 1.0 \times 10^{-3}$ since the RATTLE³² constraints are not applied. In terms of time marching method, the velocity-Verlet type algorithm^{17,37} is applied to the present study. All the CG simula-

TABLE IV. Computational conditions for the CG simulations

Parameter	Value
$(\sigma_{\text{cg}}, \epsilon_{\text{cg}})$	See Table II
CG mass, M/m_{atom}	4, 8, 12
Computational domain	Cube
Boundary	Periodic for all the directions
Side length of domain, l/σ_{atom}	26.80, 33.76, 38.56
Cutoff radius, R_C/σ_{atom} (Eq.(9))	7
Coarse-graining degree, n_{cg}	4, 8, 12
Number of CG particles in the system, N_{cg}	3375
Number density of CG particles, ρ_{cg}	0.175, 0.0876, 0.0584
System temperature, $k_B T_{\text{cg}}/\epsilon_{\text{atom}}$	1.083, 1.051, 1.032
Time increment, $\Delta t/t_{\text{atom}}$	1.0×10^{-3}

360 tions are conducted by Molly.jl³⁵, same as the MD simulations, with modifications to include the
 361 the GINH thermostat¹⁷.

362 Each CG simulation was confirmed by evaluating the conservation properties of the energy
 363 function¹⁷. The analysis demonstrated that the kinetic and potential energies of both the CG
 364 system and the NH thermostat remain statistically stable over time, with fluctuations of at most
 365 3.5% relative to their averaged values. Furthermore, the total linear momentum is conserved to
 366 within approximately 10^{-13} accuracy, ensuring that no artificial drift or systematic energy injection
 367 occurs in the system.

368 **B. Link between Q_ξ and spectral characteristics of ξ**

369 First, the relationship between the thermal inertia Q_ξ and the spectral characteristics of ξ is in-
 370 vestigated in order to find a value that can reproduce the ξ behavior of the MD simulations as pre-
 371 cise as possible. The values of σ_{cg} used in this investigation are $\sigma_{\text{cg}}/\sigma_{\text{atom}} = (1.735, 2.221, 2.574)$
 372 for $n_{\text{cg}} = (4, 8, 12)$, respectively. These are chosen such that the self diffusion coefficients of the
 373 CG systems in the CG simulations correspond to those in the MD simulations by performing a
 374 series of CG simulations. For the details of adjusting the LJ parameters, please refer to Appendix

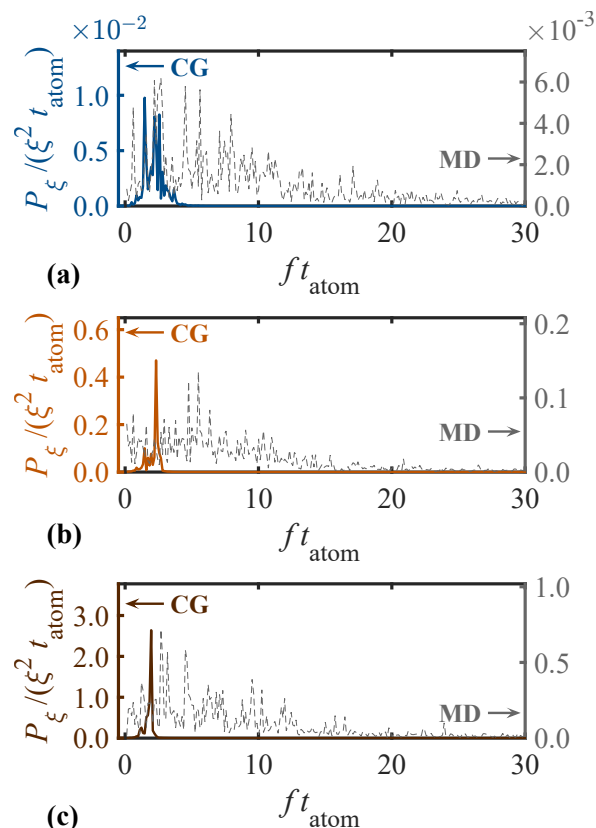


FIG. 9. Spectral characteristics of power density of ξ obtained from the CG simulations for (a) $n_{cg} = 4$, (b) 8, and (c) 12, respectively.

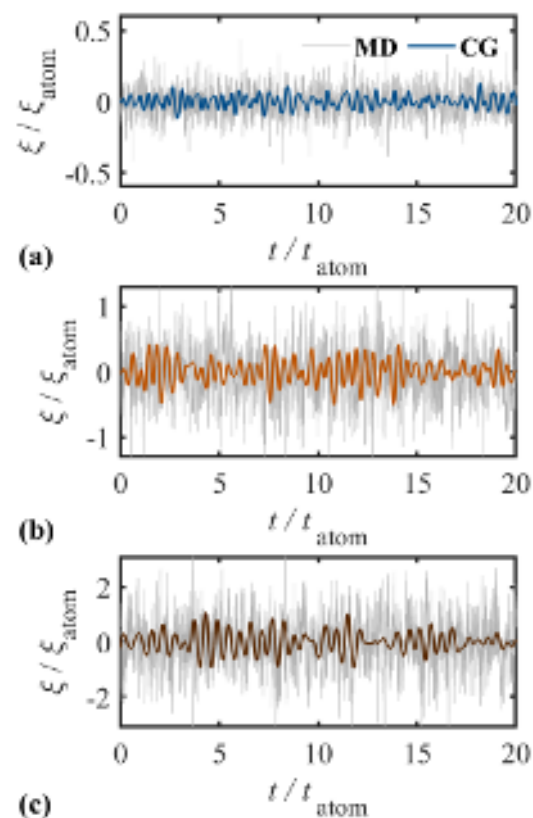


FIG. 10. History of thermostat coefficient, ξ , obtained from the CG simulations: (a), (b), and (c) are the histories with the range of $t/t_{atom} \leq 20$ for $n_{cg} = 4, 8$, and 12, respectively. The corresponding MD results shown in Figure 7 are presented in gray solid lines for comparison.

375 C.

376 Figure 9 illustrates that the spectral characteristics of ξ for different CG degrees obtained from
377 the CG simulations, where $Q_{\xi}^* = (487.8, 34.84, 10.45)$ yielding the maximum peak frequency of ξ ,
378 f_{max} , at $f_{max} t_{atom} \approx 2.5$ (see Appendix D for a more detailed discussion on the relationship between
379 Q_{ξ} and f_{max}). The gray dashed lines in the figure represent the data obtained from the correspond-
380 ing MD simulations shown in Figure 8. It is revealed from the figure that ξ for the CG simulations
381 oscillates within a much more limited frequency range compared to the MD simulations. This is
382 attributed to the nature of the NH thermostat, in which the system temperature is controlled in a
383 harmonic manner.

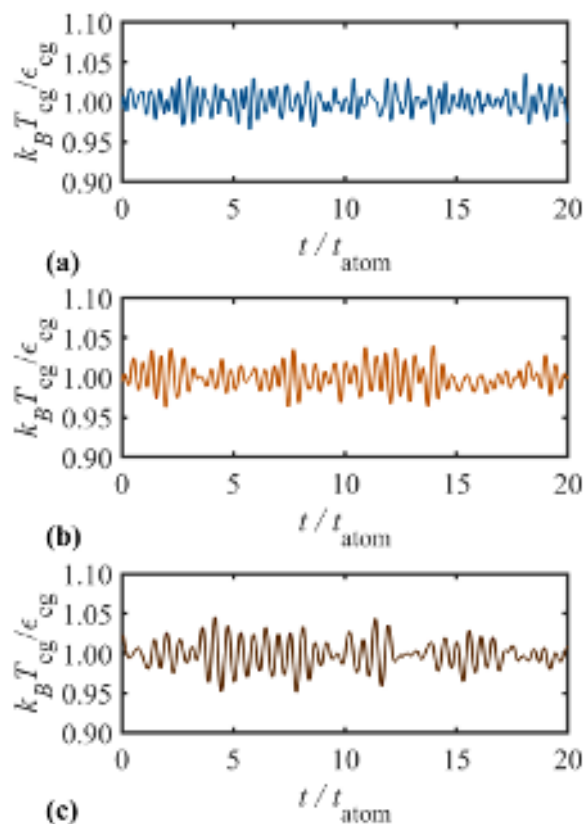


FIG. 11. Temperature history of the CG systems, $k_B T_{cg}$, for (a) $n_{cg} = 4$, (b) $n_{cg} = 8$, and (c) $n_{cg} = 12$.

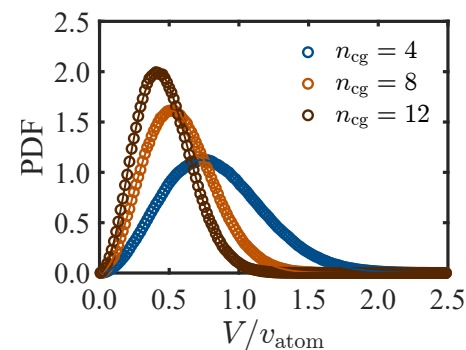


FIG. 12. Probability density function (PDF) of the speed for the CG systems obtained from CG simulations for $n_{cg} = 4$ (blue), $n_{cg} = 8$ (orange), and $n_{cg} = 12$ (dark orange).

When comparing the frequency ranges in the simulations with different CG degrees, the range is observed to become narrower as the CG degree increases. This can be associated with the mobility of CG particles as follows: As observed in the MD simulations, a CG system with higher CG degree becomes more structured, and this applies to the CG simulations as well (see Figure 14 discussed in the later section). In this structured system, CG particles move in relatively regular cycles compared to the system with lower CG degrees, resulting in the oscillation of ξ composed of a limited range of frequencies.

From the temporal history of the ξ for $n_{cg} = 4, 8$, and 12 shown in Figure 10, it is evident that the ξ oscillates in a more regular manner than the MD simulations and that the amplitudes are smaller than those for the MD simulations. In addition, it can be seen from the figure that the oscillation includes some undulation because it is composed of a limited number of oscillation modes. This can be attributed to the nature of the NH type thermostat that connects to the system with single spring to control the system temperature.

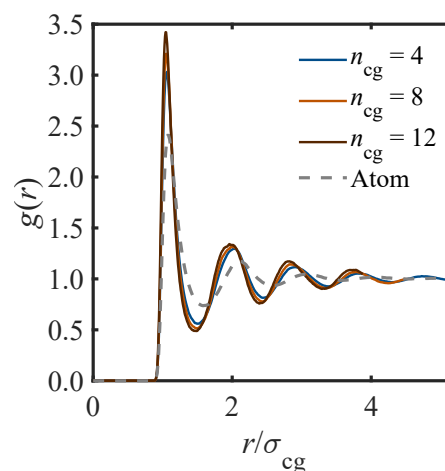


FIG. 13. Radial distribution function, $g(r)$, of the CG systems for $n_{cg} = 4$ (blue), $n_{cg} = 8$ (orange), and $n_{cg} = 12$ (dark orange).

C. CG characteristics obtained from the CG systems

In this section, the characteristics of CG system obtained from CG simulations are analyzed. The basic computational conditions for the simulations listed in Table IV are not changed. Also, based on the parametric study in the previous section, the Q_ξ values are chosen such that the fundamental frequencies for ξ fluctuation become $f_{\max} t_{\text{atom}} \approx 2.5$.

Figure 11 shows the temperature histories of the CG systems for the different CG levels. As shown in the figure, the temperature of the system fluctuates within approximately $\pm 5\%$ of the set value for all the CG-degree cases. Furthermore, it can be observed that the temperature fluctuates more regularly when compared with the MD simulations. These fluctuations in temperature correlate with those in ξ shown in Figure 10, clearly indicating that the temperature is effectively controlled by the GINH thermostat.

To further validate the equilibrium properties of the CG simulations, we analyze the probability density function (PDF) of the speed obtained from the CG simulations. Figure 12 presents the speed distributions for the CG systems with $n_{cg} = 4, 8$, and 12, where the circles indicate the computed values and the solid lines represent the theoretical Maxwell-Boltzmann distribution. The results demonstrate that the computed distributions are in good agreement with the theoretical predictions, confirming that the CG simulations maintain a proper equilibrium state.

Figure 13 presents the radial distribution functions, $g(r)$, obtained from the CG simulations with different CG degrees, where the function for the atomic system is plotted with a gray dashed

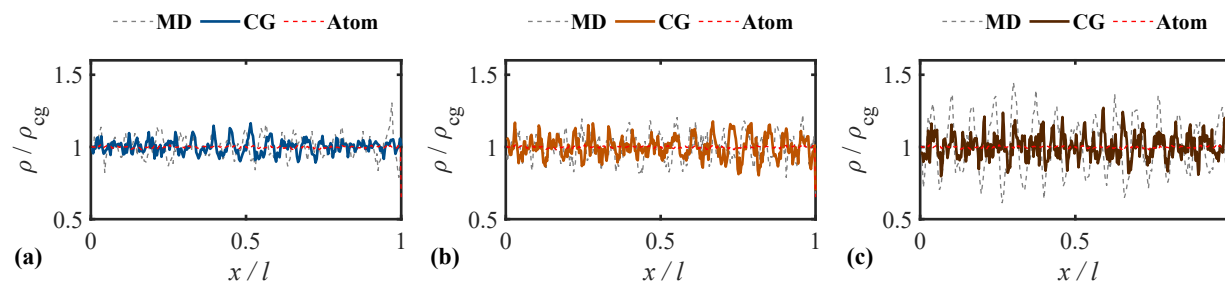


FIG. 14. Density distribution of the CG systems for (a) $n_{cg} = 4$ (blue), (b) $n_{cg} = 8$ (orange), and (c) $n_{cg} = 12$ (dark orange).

line. It should be noted that the horizontal axis r for each CG result is normalized by the corresponding σ_{cg} . From the figure, it is evident that the distributions in the CG calculations exhibit pronounced peaks, which significantly differ from the flatter distributions of Figure 2(b) obtained by the MD simulations. These distribution shapes more closely resemble that of the atomic system, suggesting that the differences in the $g(r)$ shapes between the CG and MD simulations are due to the use of the LJ potential in the CG simulations. Furthermore, it is clearly observed that the $g(r)$ distributions for the different CG degrees are approximately identical to each other. Therefore, combining this with the results from Figure 11, it can be concluded that the structural characteristics of the CG system are mostly dependent on the LJ potential, and the effect of the GINH thermostat is minimal.

The spatial distributions of the number density of CG particles for the CG simulations are plotted as a function of the x -direction in Figure 14. As is observed in this figure, the trends of the distributions are qualitatively very similar to those of the MD simulations (see Figure 4). For example, the spatial density fluctuation is much larger than that for the atomic system, and it increases as n_{cg} increases, while the change in fluctuation with increasing n_{cg} in the CG simulations is observed to be smaller than that in the MD simulations. These observations indicate that the CG simulations are able to reproduce the characteristics of the CG system obtained from the MD simulations; that is, the CG system becomes more structured as the CG degree increases.

D. Comparisons of dynamic properties of the CG system between the model and the reference

In this section, we compare the dynamic properties of the system obtained from the MD and CG simulations, and evaluate the reproducibility of the CG system by the proposed model. Specif-

ically, using the Green-Kubo relations, we calculate the self-diffusion coefficients and shear vis-
 cosities of CG particles from their velocity autocorrelation and shear stress autocorrelation coef-
 ficients, respectively. Additionally, we estimate the Schmidt number from the obtained values to
 verify the reproducibility of fluid properties in the CG system.

Diffusive characteristics

The diffusion coefficient is given by the following form based on the Green-Kubo relation¹:

$$D = \frac{1}{3} \int_0^\infty \langle \mathbf{V}(t) \cdot \mathbf{V}(0) \rangle dt, \quad (18)$$

where $\langle \mathbf{V}(t) \cdot \mathbf{V}(0) \rangle$ is the equilibrium velocity autocorrelation function (VACF), C_v , of CG parti-
 cles averaged over all the CG particles in the system. The VACF was computed using the Wiener-
 Khinchin theorem with fast Fourier transform (FFT). To minimize statistical noise, Welch's
 method was applied, ensuring improved statistical accuracy over long correlation times. We
 have confirmed that the obtained diffusion coefficient is not affected by the simulation duration.

Figure 15 shows the VACFs obtained from the MD and CG simulations, where it should be
 noted that the horizontal axes are the time normalized by LJ properties for each CG simulation.
 From this figure, we first observe that the VACFs for the MD simulations diminish more rapidly
 than those for the CG simulations. Additionally, no negative correlations are observed in the MD
 simulations, whereas they are presented in the CG simulations. Despite slight shape differences
 due to variations in CG degrees, the VACFs in both simulations are well organized over time when
 normalized based on the LJ parameters of the CG particles. These observations clearly indicate
 that the VACF is primarily influenced by the absence of many-body effect in the CG simulations
 attributed to the simple modeling of the inter-CG potential force, which largely accounts for the
 differences between the functions observed in the MD and CG simulations.

Another index representing diffusive characteristics of particle system is the mean square dis-
 placement, MSD, which is expressed as¹:

$$\text{MSD} = \langle |\mathbf{R}(t) - \mathbf{R}(0)|^2 \rangle. \quad (19)$$

Figure 16 shows the MSDs as a function of time normalized by the atomic time scale for the differ-
 ent CG degrees, where the left and right figures are presented with double logarithmic and linear
 scales, respectively. As illustrated in the figure, the MSDs derived from both the MD simulations

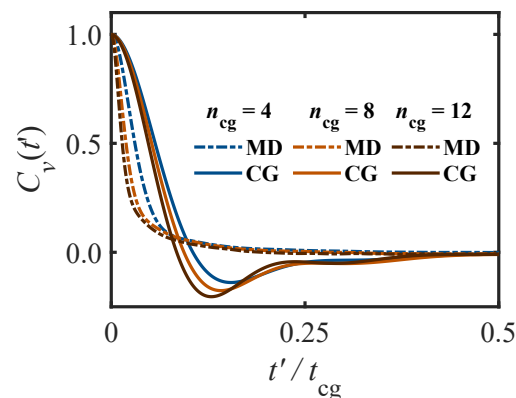


FIG. 15. Velocity autocorrelation functions, C_v , of CG particles obtained from the MD and CG simulations for different CG degrees. t_{cg} : Time scale based on the LJ parameters for each CG degree.

and the CG simulations align remarkably well for all the CG degrees. Although minor differences can be seen in the linear scale plot (right figure), from the logarithmic scale plot, it is evident that the short- to long-term behaviors of CG particles in the MD simulations are accurately reproduced by the CG simulations. As mentioned earlier, the σ_{cg} values for each CG level were determined to ensure that the diffusion coefficients, calculated using Eq.(18), correspond with those obtained from the MD simulations, despite not considering the MSDs in this determination.

Viscous characteristics

The shear viscosity is given by the following form based on the Green-Kubo relation¹:

$$\mu = \frac{V}{k_B T} \int_0^\infty \langle S_{\alpha\beta}(t) \cdot S_{\alpha\beta}(0) \rangle dt. \quad (20)$$

$S_{\alpha\beta}$ is given by¹

$$S_{\alpha\beta} = \frac{1}{V} \left[\sum_{\eta} \left(\frac{P_{\eta,\alpha} P_{\eta,\beta}}{M_{\eta}} \right) + \sum_{\eta} (R_{\eta,\alpha} F_{\eta,\beta}) \right], \quad (21)$$

and is the off-diagonal $\alpha\beta$ element of stress tensor, that is, $\alpha \neq \beta$. In this case, $\langle S_{\alpha\beta}(t) \cdot S_{\alpha\beta}(0) \rangle$ is the equilibrium shear stress autocorrelation function (SACF), C_{SS} , of CG particles averaged over all the CG particles in the system. The pressure or normal stress can also be calculated using Eq.(21) with $(\alpha = \beta)$. $F_{\eta\beta}$ is the β component of the interparticle forces acting on η th CG particle, \mathbf{F}_{η} , where $\mathbf{F}_{\eta} = \sum_k^{n_{cg}} \left[-\frac{\partial U(\mathbf{q})}{\partial \mathbf{q}_{(\eta,k)}} \right]$ for the MD simulation and $\mathbf{F}_{\eta} = -\frac{\partial \bar{U}(\mathbf{R})}{\partial \mathbf{R}_{\eta}}$ for the CG simulations.

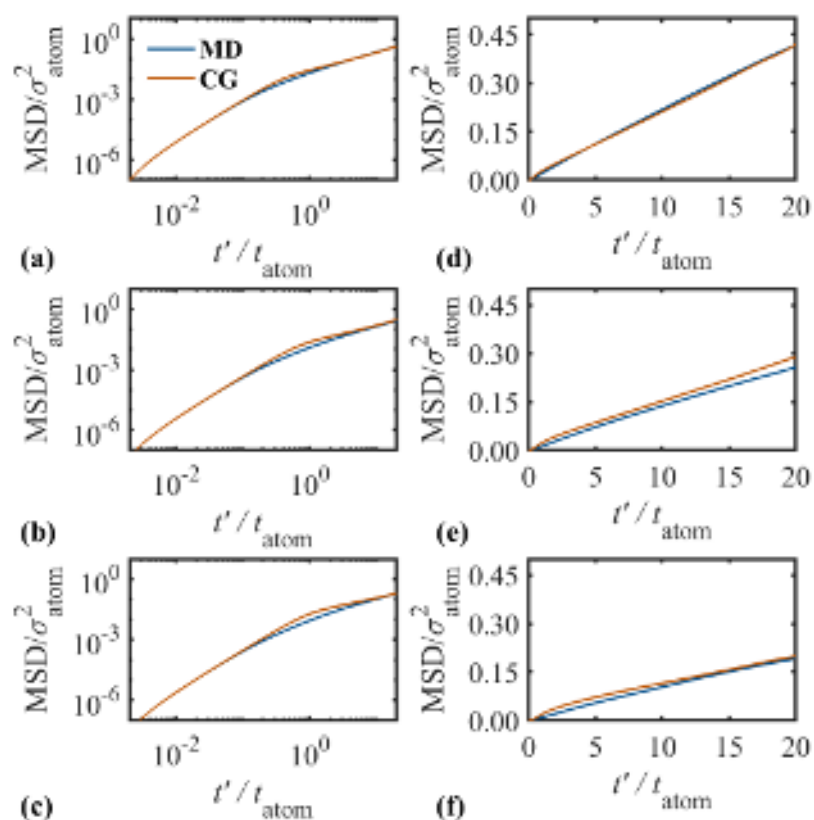


FIG. 16. Mean square displacement, MSD, for different CG levels. Left figures: (a), (b), and (c) are for $n_{cg} = 4, 8, \text{ and } 12$, respectively, presented with log-scale axes. Right figures: (d), (e) and (f) are the corresponding results of (a), (b), and (c) presented with linear-scale axes.

First, the temporal histories of pressure and shear stress for the MD and CG simulations are examined. Figure 17 shows the comparisons of pressure (xx element, S_{xx}) and shear stress (xy element, S_{xy}) between the MD and CG simulations for different CG degrees, where the results from the MD simulations are plotted with gray lines. It can be seen from this figure that, for both MD and CG simulations, the pressure (Figure 17 (a), (b), and (c)) remains constant during the duration of the simulations regardless of the CG degrees. When comparing the results between the MD and CG simulations, the pressure fluctuations for the CG simulations are much smaller than those for the MD simulations, which is due to the absence of many-body effects in the MD simulations. Also, it is revealed that the time-averaged values vary depending on the CG degrees for the CG simulations while these are approximately the same for the MD simulations. However, the overall average values roughly range between 0.5 and 0.8. This is considered to be due to the application of the LJ potential to the inter-CG potential. Previous studies^{28,38,39} have shown that

Nosé-Hoover Dynamics for CG in Lennard-Jones Systems

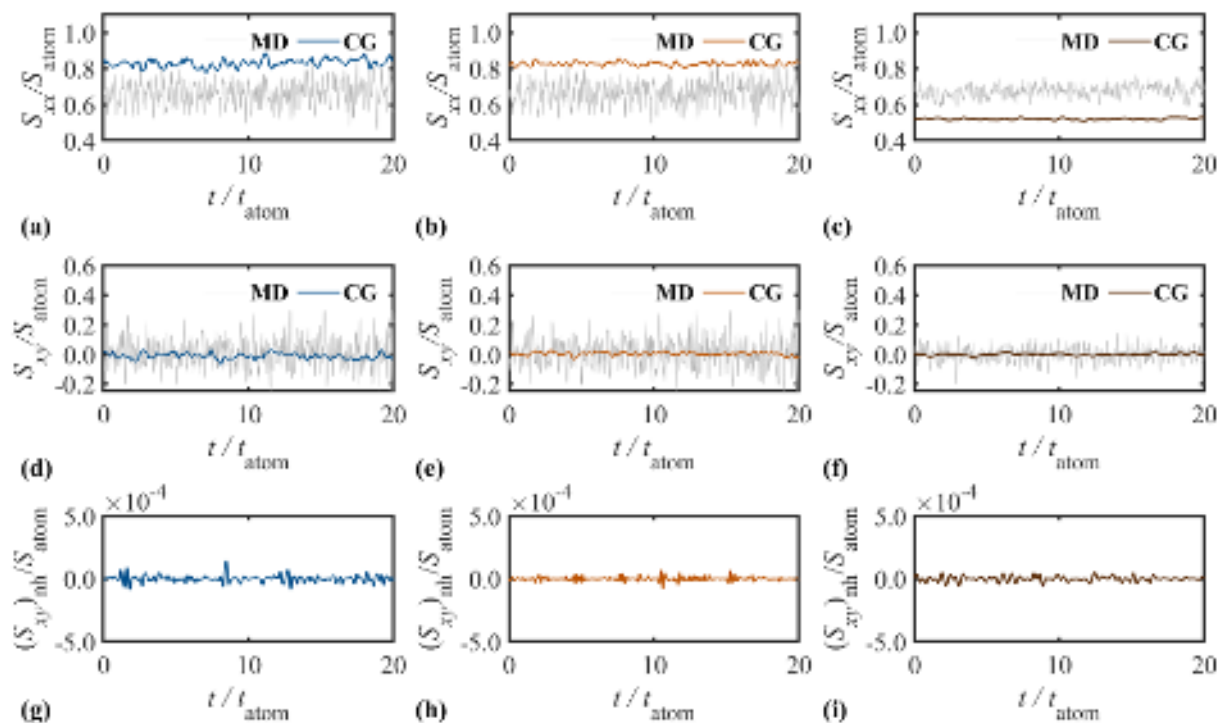


FIG. 17. Normal and shear stress time histories of CG systems with different CG levels. (a), (b), and (c): Normal stress (pressure). (d), (e), (f): Shear stress (kinetic and LJ potential terms). (g), (h), and (i): Shear stress (GINH term). $n_{cg} = 4$ (blue), $n_{cg} = 8$ (orange), and $n_{cg} = 12$ (dark orange) for the results of the CG simulations, and gray lines for the results of the MD simulations.

accurately reproducing the inter-CG potential leads to an underestimation of the system pressure, necessitating corrections to the potential forces. The use of LJ potential may be a possible option to reproduce the pressure of reference systems in case that the structural characteristics are not important, e.g., solvent of a suspension liquid.

The trend of the shear stress is approximately the same as that of the pressure as revealed in Figure 17 (d), (e), and (f). In contrast to the pressures varying depending on CG degrees for the CG simulations, the shear stresses remain zero for all the simulation cases. The contribution of the GINH thermostat to shear stress is also evaluated by extracting the second term of Eq.(21) and let $\mathbf{F}_\eta = -\xi \mathbf{V}_\eta$, namely,

$$(S_{\alpha\beta})_{nh} = \frac{1}{V} \sum_{\eta} [R_{\eta,\alpha} (-\xi \mathbf{V}_{\eta,\beta})] . \quad (22)$$

The temporal histories of this value for different CG degrees are shown in Figure 17 (g), (h), and (i), demonstrating that the magnitude of the fluctuation is about one thousandth of that of the shear

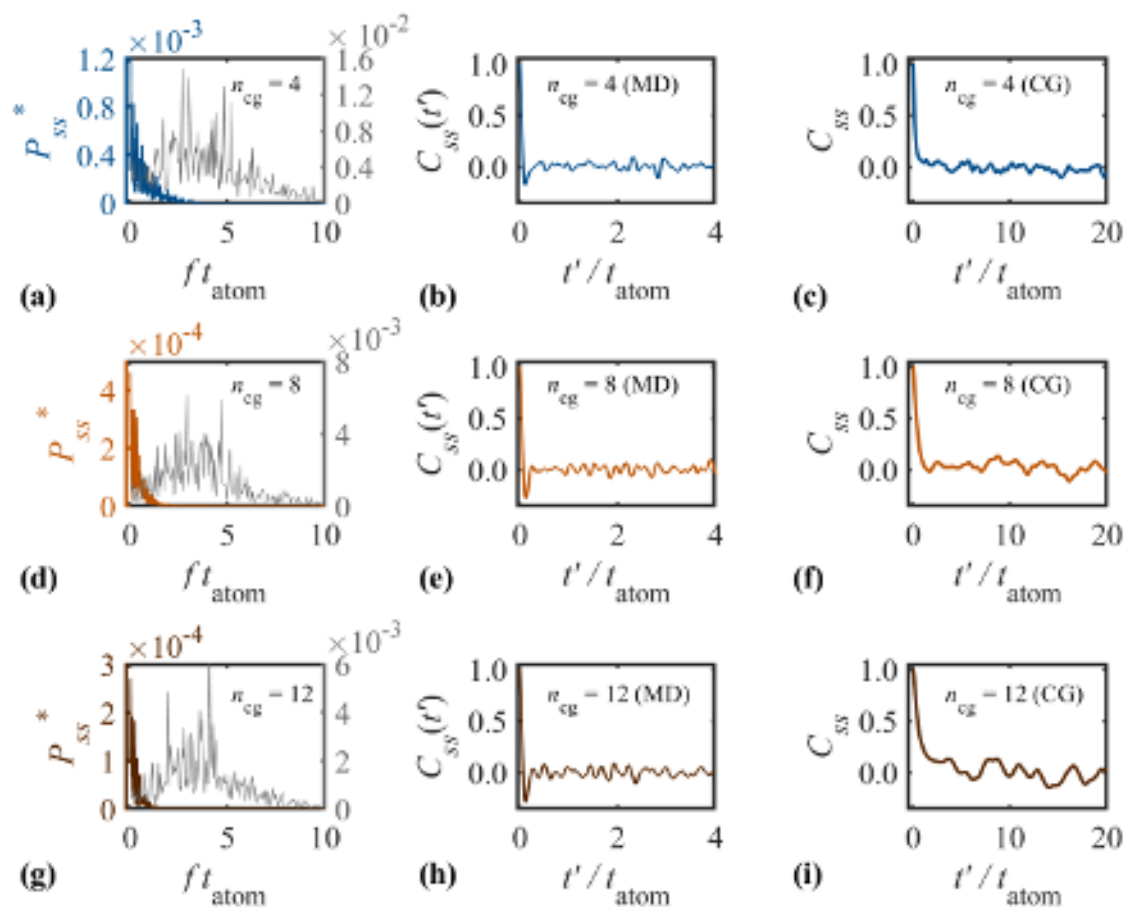


FIG. 18. Spectral characteristics and autocorrelation function of shear stresses, C_{ss} , for CG systems. (a), (d), and (g): Power density as a function of frequency. Gray lines are the results of the MD simulations, and colored lines are those of the CG simulations. (b), (e), and (h): C_{ss} obtained from the MD simulations. (c), (f), (i): C_{ss} obtained from the CG simulations. $n_{cg} = 4$ (blue), $n_{cg} = 8$ (orange), and $n_{cg} = 12$ (dark orange), for all the subfigures. P_{ss}^* : Normalized value of power density of $S_{\alpha\beta}$, P_{ss} ($P_{ss}^* = P_{ss}/(S_{atom}^2 t_{atom})$)

).

stress (S_{xy}) and thus the GINH thermostat makes little contribution to shear stress.

Next, the spectral characteristics and autocorrelation functions of the shear stress for different CG degrees are compared between the MD simulations and the CG simulations, which are shown in Figure 18. When comparing the power spectrum between the MD and CG simulations, it can be clearly observed that the shear stresses for the CG simulations fluctuate with the normalized frequencies of $f t_{atom} < 4$ and those of $f t_{atom} < 1$ are dominated. On the other hand, the fluctuations of the MD simulations consist of a wider frequencies of $f t_{atom} < 10$ and are prominent at the frequency region of $2 < f t_{atom} < 5$. This quantitatively demonstrates the difference in the temporal

516 fluctuations shown in Figure 17. The dominant frequencies of the CG simulations are not well
 517 correlated with those for the thermostat coefficient ξ , indicating that the stress field is developed
 518 mainly due to the potential force.

519 The SACFs obtained based on the spectral data for the MD and CG simulations are illustrated
 520 in Figure 18 (b), (e), and (h), and (c), (f), and (i), respectively. For the calculation of SACF, the
 521 Wiener-Khinchin theorem with FFT was used, and statistical noise was reduced using Welch's
 522 method, similar to the VACF calculation.

523 It is observed from these figures that, for both simulations, the correlation exhibits oscillations
 524 after it declines to approximately zero. Comparing these two simulations, the time interval of
 525 oscillations for the CG simulations is larger than those for the MD simulations. Next, focusing on
 526 the effect of CG degree, the oscillation time interval increases as CG degree becomes greater. This
 527 corresponds to the ranges of the power spectrum becoming narrower as CG degree increases. The
 528 time interval for the MD simulations does not appear to be affected by the degree.

529 Finally, the reproducibility of kinematic characteristics for the present CG method is evaluated
 530 with self diffusivity, kinematic viscosity, and Schmidt number.

531 The diffusivity and the shear viscosity are calculated with using Eqs.(18) and (20), respectively.
 532 For the viscosity, fitted curves estimated in Appendix E are used to eliminate the influence of os-
 533 cillations in the tail part of the correlation function. Then, the kinematic viscosity, ν , is calculated
 534 with $\nu = \mu / \rho_m$ where ρ_m is the density of the system.

535 Table V show the summary of the dynamic properties obtained by the present study. It can be
 536 confirmed from the table that there exist the differences between the computed shear viscosities
 537 and those obtained from the fitting curves for all the simulations although their magnitudes varies.
 538 This indicates that the effect of the oscillation in the tail is eliminated in the values with fitting
 539 curves.

540 Next, the Sc values obtained in this study are compared with those reported by Lei et al.²¹. Lei
 541 et al. performed coarse-graining of an LJ system using a bottom-up DPD approach²³, where the
 542 number density and the number of coarse-grained particles were similar to those in the present
 543 study. In their CG simulations, the Sc values in the CG system obtained from MD simulations
 544 ranged from approximately 10 to 400. The corresponding CG simulations reproduced the Sc
 545 values within the same order of magnitude, although under certain conditions, Sc values as high as
 546 10^4 were observed. As can be seen in Table V, the reproducibility of Sc values in the present study
 547 is comparable to that reported by Lei et al.²¹, indicating that both approaches have the ability to

TABLE V. Dynamic characteristics for the CG systems with different CG levels

n_{cg}	MD / CG	$D/D_{\text{atom}} (\times 10^{-3})$	ν/ν_{atom}	Sc
4	MD	31.51	22.38	710
	MD (fit)		4.577	145
	CG	31.75	1.725	54.3
	CG (fit)		3.723	116
8	MD	20.65	6.768	342
	MD (fit)		2.729	138
	CG	19.77	6.097	295
	CG (fit)		6.646	321
12	MD	14.52	3.203	220
	MD (fit)		2.598	179
	CG	14.77	1.859	126
	CG (fit)		3.977	269

548 achieve Sc values of similar feasibility.

549 Focusing on the viscosities obtained from the fitting curves, the comparisons of the viscosities
 550 of the MD simulations and those of the CG simulations show that their magnitudes are in the same
 551 range. On the other hand, the difference between the two is the largest for $n_{\text{cg}} = 8$, with the ratio
 552 being more than twofold. It is considered that these differences are attributed to the fact that the
 553 LJ potential is adopted for the inter-CG-potential, \bar{U} . Such simple approximation is only able to
 554 reproduce the mass diffusion as is manifested in Figure 16 and Table V of the CG systems but it
 555 is not sufficient for the momentum diffusion.

557 The effect of the CG potential \bar{U} modeled by the LJ potential is discussed at the end. As
 558 described earlier, it was found that the GINH term did not significantly influence the physical
 559 properties in the CG simulations and it was considered that these were essentially dominated by
 560 \bar{U} . Nevertheless, the CG simulations were diverged when the potential forces were only applied
 561 with deactivating the GINH term in our preliminary simulations. Therefore, the GINH term was
 562 found to be necessary to maintain the CG system in an equilibrium state.

563 In this study, the parameters in the GINH term, including the exponent of the weight function,
 564 were set to be the same as the previous study. This exponent has been known to be relevant to

the dynamic properties in the dissipative particle dynamics. Thus the same can be assumed for the GINH term because it has the same form as the dissipative term in the DPD. The modification of this value, along with the improvement of the associated potential function, is expected to enhance the reproducibility of both structural and dynamic properties. This further investigation is left for our future work because the main focus of the present study is on applying the GINH thermostat to molecular coarse-graining.

V. CONCLUDING REMARKS

In this study, a coarse-grained (CG) model based on the Nosé-Hoover (NH) dynamics was proposed. The NH dynamics is often used in the molecular dynamics (MD) simulations in order to maintain temperature of the computational system constant as a thermostat. In this study, the equation of motion (EOM) of a CG particle based on the atomic system was associated with that including the NH term. The relationship between the thermostat parameters and the MD potential forces was then derived.

A set of MD simulations was performed to evaluate the NH parameters, ξ and Q_ξ , for different CG levels, where the monoatomic systems governed only by the Lennard-Jones (LJ) potential were considered. The results showed that the ξ value oscillated around zero over time. Also, the spectral analysis of the ξ values revealed that its oscillations were mainly composed of frequencies that are less than ten times the frequency scale derived from the LJ parameters for the atomic system. Regarding the Q_ξ value, it was derived by using the calculated ξ values based on the least squares method. However, the obtained values were unsuitable for accurately replicating the peak frequencies of ξ in the CG simulations.

A set of CG simulations was then performed to reproduce the dynamic properties of the MD system. First, a set of parametric computations was conducted to evaluate the relationship between the Q_ξ value and the temporal characteristics of ξ . It was shown that Q_ξ was proportional to the square of the peak frequency of ξ , which was the same as that in the standard NH dynamics. Additionally, it was confirmed in the CG simulations that the oscillations of ξ were consisted of frequencies with a narrower range compared to the MD simulations. This characteristic is attributed to the time evolution equation of ξ , which generates its fluctuations in a harmonic manner¹⁷. One approach to minimize the discrepancy between the MD and CG simulations is to use Nosé-Hoover Chain (NHC) type dynamics. This method was initially introduced to address the lack of ergod-

595 icity in the NH dynamics. In the NHC dynamics, different thermostats are linked in a sequential
596 chain, allowing a wider range of frequencies to be included in the ξ fluctuations. This may lead to
597 a more accurate reproduction of ξ behavior in the CG simulations.

598 The dynamic properties obtained from the CG simulations were finally compared to those of
599 the MD simulations. The self diffusivity of the CG system in the CG simulation was tailored to
600 accord it with that in the MD simulation by controlling the LJ parameters of the inter-CG-particle
601 potential. This resulted in an excellent agreement in the mean square displacement (MSD). On the
602 other hand, the behaviors of the velocity autocorrelation function (VACF) did not coincide well
603 between those simulations.

604 For the shear viscosity, the agreement between the MD and CG simulations was not as good
605 as that for the self diffusivity where the largest difference confirmed was more than twofold. The
606 oscillation was observed in the tail of the shear stress autocorrelation function for both the MD
607 and CG simulations unlike the VACF, which may have prevented accurate calculation of the shear
608 viscosity although the viscosity was calculated by using the fitting function to reduce the effect.

609 In future work, it is planned to modify the model of the inter-CG-potential and the thermostat
610 part such that both mass and momentum diffusions can be approximated well in the CG simula-
611 tions as well as that this CG method becomes further applicable to the CG systems with higher
612 degree of coarse-graining.

613 ACKNOWLEDGEMENT

614 This research was supported by the Japan Society for the Promotion of Science (JSPS) KAK-
615 ENHI Grant Number JP22K03904.

616 AUTHOR CONTRIBUTIONS

617 TY: Conceptualization, Data curation, Formal analysis, Funding acquisition, Investigation,
618 Methodology, Project administration, Resources, Software, Validation, Visualization, Writ-
619 ing - original draft, Writing - review & editing.

620 YM: Supervision, Resources, Writing - review & editing.

621 CONFLICT OF INTEREST

622 The authors have no conflict to disclose.

623 DATA AVAILABILITY

624 The data that support the findings of this study are available from the corresponding author
625 upon reasonable request.

626 Appendix A: Normalizing factors for simulation variables

Length	σ_{atom}
Energy	ϵ_{atom}
Mass	m_{atom}
Time	$t_{\text{atom}} = \sqrt{m_{\text{atom}} \sigma_{\text{atom}}^2 / \epsilon_{\text{atom}}}$
Density	σ_{atom}^3
Force	$F_{\text{atom}} = \epsilon_{\text{atom}} / \sigma_{\text{atom}}$
Thermostat coefficient	$\xi_{\text{atom}} = \epsilon_{\text{atom}} t_{\text{atom}} / \sigma_{\text{atom}}^2$
Momentum inertia	$Q_{\xi, \text{atom}} = \sigma_{\text{atom}}^4 / t_{\text{atom}}^2 / \epsilon_{\text{atom}}$
Diffusivity	$D_{\text{atom}} = \sigma_{\text{atom}}^2 / t_{\text{atom}}$
Pressure and stress	$S_{\text{atom}} = \epsilon_{\text{atom}} / \sigma_{\text{atom}}^3$
Kinematic viscosity	$\nu_{\text{atom}} = \sigma_{\text{atom}}^2 / t_{\text{atom}} = D_{\text{atom}}$

627 Appendix B: Estimation of Q_{ξ} using the least square method

628 In this study, the Q_{ξ} value was first estimated by using the MD data with the following pro-
629 cedure. Eq.(12) gives the temporal history of ξ for each coarse-grained particle. Meanwhile, the
630 discrete form of Eq.(10) with the explicit Euler method can be expressed as

$$631 \frac{\xi_{\alpha}^{n+1} - \xi_{\alpha}^n}{\Delta t} = Q_{\xi}^{-1} \left(\sum_{\eta} \sum_{\theta > \eta} \left\{ W(R_{\eta\theta}) \left[\left(\mathbf{V}_{\eta\theta} \cdot \hat{\mathbf{R}}_{\eta\theta} \right)^2 - k_B T / M_{\eta\theta} \right] \right\} \right)^n, \quad (\text{B1})$$

where n is the temporal step number, and α is the index of CG particles. Based on this equation, ξ_α^{n+1} can be obtained by

$$\xi_\alpha^{n+1} = \xi_\alpha^n + Q_\xi^{-1} \times \Delta t G^n, \quad (\text{B2})$$

where

$$G^n = \left(\sum_\eta \sum_{\theta > \eta} \left\{ W(R_{\eta\theta}) \left[(\mathbf{v}_{\eta\theta} \cdot \hat{\mathbf{R}}_{\eta\theta})^2 - k_B T / M_{\eta\theta} \right] \right\} \right)^n. \quad (\text{B3})$$

The Q_ξ value is estimated in such a way that the sum of the squared discrepancy of ξ_α^{n+1} between Eq.(12) and Eq.(B2), S_{err} , is minimized with using the least square method.

S_{err} can be written as

$$S_{err} = \sum_n \sum_\alpha \left([\xi_\alpha^{n+1}]_{\text{Eq.(12)}} - [\xi_\alpha^{n+1}]_{\text{Eq.(B2)}} \right)^2, \quad (\text{B4})$$

where $[\xi_\alpha^{n+1}]_{\text{Eq.(\#)}}$ indicates the ξ_α^{n+1} value estimated by using Eq.(#) (# : 12 or B2). $\frac{\partial S_{err}}{\partial Q_\xi^{-1}} = 0$ satisfies the above estimation condition. Thus,

$$\begin{aligned} \frac{\partial S_{err}}{\partial Q_\xi^{-1}} &= 2 \sum_n \sum_\alpha \left([\xi_\alpha^{n+1}]_{\text{Eq.(12)}} - [\xi_\alpha^{n+1}]_{\text{Eq.(B2)}} \right) \left(-\frac{\partial [\xi_\alpha^{n+1}]_{\text{Eq.(B2)}}}{\partial Q_\xi^{-1}} \right) \\ &= -2\Delta t \sum_n \sum_\alpha \left([\xi_\alpha^{n+1}]_{\text{Eq.(12)}} - [\xi_\alpha^{n+1}]_{\text{Eq.(B2)}} \right) G^n \\ &= 0. \end{aligned} \quad (\text{B5})$$

Substituting Eq.(B2) into above equation gives

$$Q_\xi^{-1} = \frac{\sum_n \left[G^n \sum_\alpha \left([\xi_\alpha^{n+1}]_{\text{Eq.(12)}} - [\xi_\alpha^n]_{\text{Eq.(B2)}} \right) \right]}{\Delta t N_{\text{cg}} \sum_n (G^n)^2}. \quad (\text{B6})$$

The results of the Q_ξ estimation for the MD simulations of different CG levels has been shown in Table III, manifesting that the values are not appropriate to reproduce the spectral characteristics of ξ in the CG simulations as described in the main part of the paper.

Appendix C: Adjusting the σ_{cg} for the CG systems

As stated in Section IV B, the values of σ_{cg} used in this investigation are chosen such that the self diffusion coefficients of the CG systems in the CG simulations correspond to those in the MD simulations by performing a series of CG simulations. It can be easily inferred that increasing the

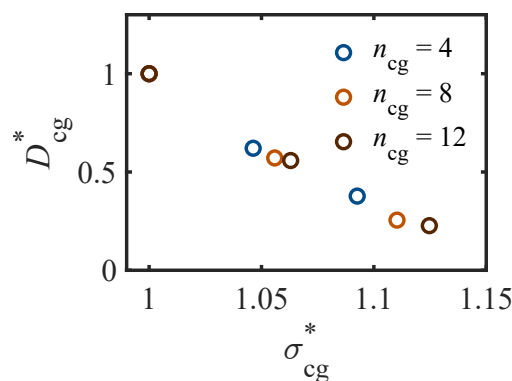


FIG. 19. Calculated diffusion coefficient, D_{cg} , as a function of σ_{cg} .

LJ parameter σ_{cg} extends the interaction range between particles, which restricts particle motion due to enhanced intermolecular interactions, thereby reducing the diffusivity. In this study, we considered this dependency and adjusted the LJ parameters to achieve consistency in diffusion coefficients between CG and MD simulations by parametrically changing the value of σ_{cg} .

Figure 19 illustrates dependency of the diffusivity on the σ_{cg} for different CG degrees, in which $\sigma_{cg}^* = \sigma_{cg}/\sigma_{cg,Eq.(17)}$ and $D_{cg}^* = D_{cg}/D_{cg,Eq.(17)}$ ($\sigma_{cg,Eq.(17)}$: σ_{cg} obtained by Eq.(17). $D_{cg,Eq.(17)}$: Diffusivity obtained from the CG simulation with $\sigma_{cg} = \sigma_{cg,Eq.(17)}$). As can be seen in this figure, regardless of CG level, the D_{cg} value monotonically decreases with σ_{cg} . This result confirms that the diffusivity can be parametrically adjusted by changing the σ_{cg} value. Based on this parametric CG computation, $\sigma_{cg}/\sigma_{atom} = (1.735, 2.221, 2.574)$ for $n_{cg} = (4, 8, 12)$, were found to reproduce the D_{cg} values for the different CG levels obtained by the MD simulations as shown in Table V. Comparing these values with those obtained by Eq.(17) shown in Table II, it is found that they are close to each other although it seems that σ_{cg} is better estimated with $(\sigma_{cg}/\sigma_{atom}) = 1.113 \times n_{cg}^{1/3}$.

Appendix D: Relationship between Q_ξ and fluctuation characteristics of ξ

The links between Q_ξ , f_{max} , and n_{cg} are crucially important for modeling the dynamics of CG system. In standard NH thermostat, Q_ξ and f_{max} are considered to be related to each other with $Q_\xi = N_{cg}k_B T f_{max}^{-2}$ ¹⁴, where the unit of this thermal inertia is different from that for the GINH thermostat. Thus, this relation needs to be revised for the GINH thermostat because, according to our literature survey, the relation has not become evident yet. Figure 20 shows the relationships between f_{max} and Q_ξ at different CG degrees. For $n_{cg} = 4$ (presented in blue circles), the filled point represent the average of three prominent peaks, as multiple frequency peaks were observed.

Nosé-Hoover Dynamics for CG in Lennard-Jones Systems

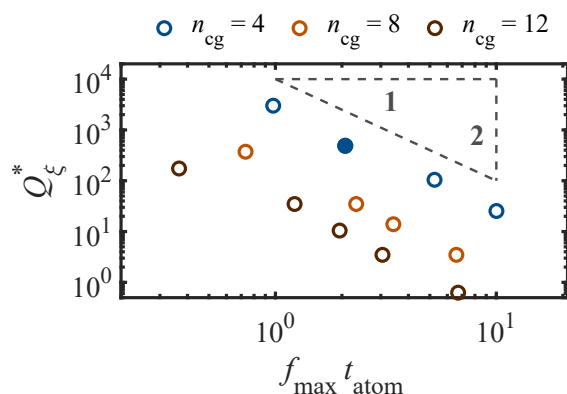


FIG. 20. Dependence of pseudo mass Q_ξ on peak frequency of $\langle \xi \rangle$ for different CG levels.

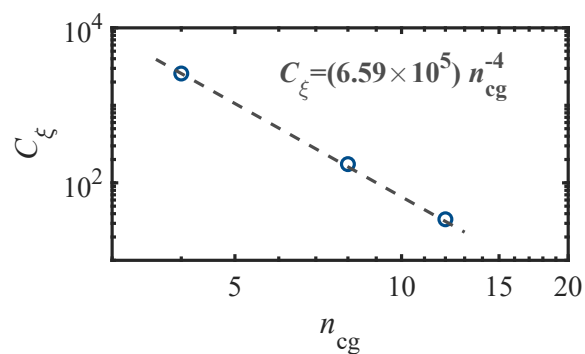


FIG. 21. Dependence of C_ξ on CG levels.

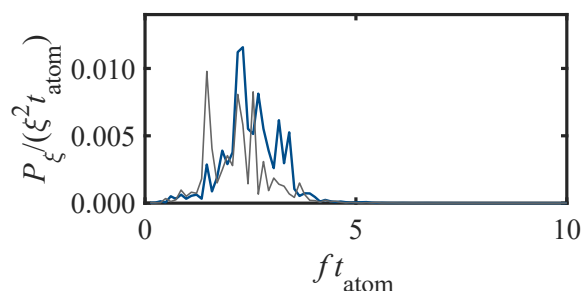


FIG. 22. Spectral characteristics of the power density of ξ obtained from the CG simulations for $n_{cg} = 4$ with $Q_\xi^* = 412.1$ calculated by $C_\xi = (6.59 \times 10^5) n_{cg}^{-4}$ (blue) and $Q_\xi^* = 487.8$ chosen via the parametric study (gray line).

From this figure, by appropriately choosing Q_ξ , it is possible to obtain fluctuation characteristics of ξ that are closer to those in MD simulations. This also explains why the least squares method failed to yield an accurate Q_ξ : the method assumes an optimal fit for average values, but it does not take into account the frequency-dependent nature of ξ 's fluctuations. Similarly, Figure 21 shows how Q_ξ scales with n_{cg} . This suggests that instead of relying solely on the least squares method, a more precise approach must consider both the frequency response and system size dependence when determining Q_ξ . These insights were crucial in refining our parameter selection for the CG simulations. This trend is exactly the same as the standard NH thermostat while the proportionality factor is not clear. Therefore, by assuming the following relationship,

$$Q_\xi^* = C_\xi (f_{\max} t_{\text{atom}})^{-2}, \quad (\text{D1})$$

the dependence of C_ξ on CG degree is estimated. Figure 21 shows the relationship between C_ξ and n_{cg} , where C_ξ for each CG level is obtained by the LSM based on Eq.(D1). From this figure, it is clearly observed that C_ξ is inversely proportional to the fourth power of n_{cg} . This relationship is expressed as $C_\xi = (6.59 \times 10^5)n_{cg}^{-4}$ as shown in Figure 21, where the proportionality constant was determined using the LSM. When this equation is applied for the estimation of thermal inertia for $n_{cg} = 4, 8$ and 12 , the values are estimated as $Q_\xi^* = 412.1, 25.75$, and 5.087 , respectively. Figure 22 shows the spectral characteristics of ξ for $n_{cg} = 4$ with using $Q_\xi = 412.1$ in blue solid line where the result for $Q_\xi^* = 487.8$ is also presented in gray solid line for comparison. As can be seen in this figure, the profiles of P_ξ using these values are highly similar to each other although the regions of the band spectra are slightly different. The difference in the maximum peak frequency based on these results is calculated to be 0.183 , indicating that Eq.(D1) can well predict Q_ξ values for arbitrary n_{cg} up to at least $n_{cg} = 12$.

Appendix E: Fitting the stress autocorrelation function

As shown in Figure 18, the C_{ss} of the CG systems for both MD and CG simulations oscillates around zero as time advances and it does not converge to zero unlike the velocity autocorrelation function shown in Figure 15. This influences the estimations of the shear viscosity based on Eq.(20). In order to avoid this effect, a fitting function is used to smooth the oscillations. The function used is a linear combination of exponentially damped curves whose form is expressed as follows:

$$C_{ss, fit} = \lambda_0 \exp\left(-\frac{t'^2_{atom}}{\tau_0}\right) \cos(\omega t'_{atom} - \phi) + \sum_{i=1}^n \lambda_i \exp\left(-\frac{t'^2_{atom}}{\tau_i}\right). \quad (E1)$$

For the MD simulation results, $n = 1$ is chosen while $n = 3$ and $\lambda = 0$ (the first term is not used for the fitting) was chosen for the CG simulation results. A similar form has been used in the previous study by Li et al.²⁶. Their study has shown that the employed fitting function successfully captures both the detailed initial behavior and the subsequent decay to zero of the fluctuating force autocorrelation function in the DPD system. To further improve the accuracy of the fit, particularly in reproducing the behavior at time zero, a slightly modified function, Eq.(E1), was introduced to the model function while maintaining its essential characteristics. Figures 23 and 24 show the comparison between the C_{ss} and the fitting curves for different CG levels of the MD and CG simulations, where the coefficients of the curves for each CG level were estimated by using the iterative least square estimation method through the MATLAB program. The parameters estimated

Nosé-Hoover Dynamics for CG in Lennard-Jones Systems

TABLE VI. Parameters in $C_{ss,\text{fit}}$ (Eq.(E1)) for fitting the computed stress autocorrelation functions for different CG levels in the MD and CG simulations.

MD / CG	n_{cg}	Index i	λ_i	τ_i^{-1}	n_{cg}	Index i	λ_i	τ_i^{-1}	n_{cg}	Index i	λ_i	τ_i^{-1}
MD	4	0	0.333	11.96	8	0	0.596	39.058	12	0	0.588	38.3
		1	1.305	329		1	0.421	575		1	0.495	384
		(ω, ϕ)	4.431	-3.513		(ω, ϕ)	20.76	-0.076		(ω, ϕ)	18.48	-0.397
CG	4	0	-	-	8	0	-	-	12	0	-	-
		1	0.442	8.388		1	0.690	3.043		1	0.413	1.488
		2	0.480	0.040		2	0.262	0.019		2	0.418	7.954
		3	0.074	0.183		3	0.049	0.005		3	0.168	0.05

717 for each CG simulation are shown in Table VI. As can be seen in this figure, the fitting curves
720 represent the initial decay of C_{ss} and smooth out the oscillations in the tail.

Nosé-Hoover Dynamics for CG in Lennard-Jones Systems

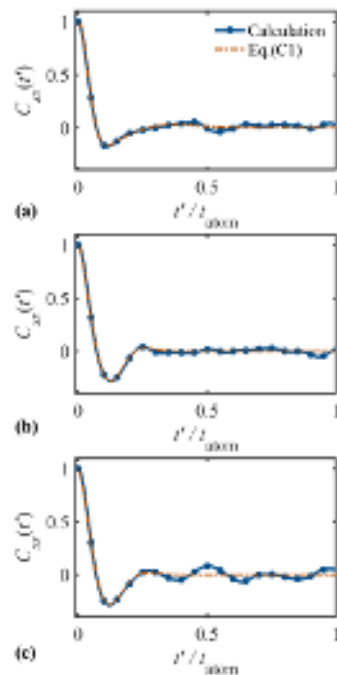


FIG. 23. Comparisons of the auto-correlation function of shear stresses, C_{ss} , for CG systems in the MD simulations with the fitting curves based on Eq.(E1) for different coarse-graining levels.

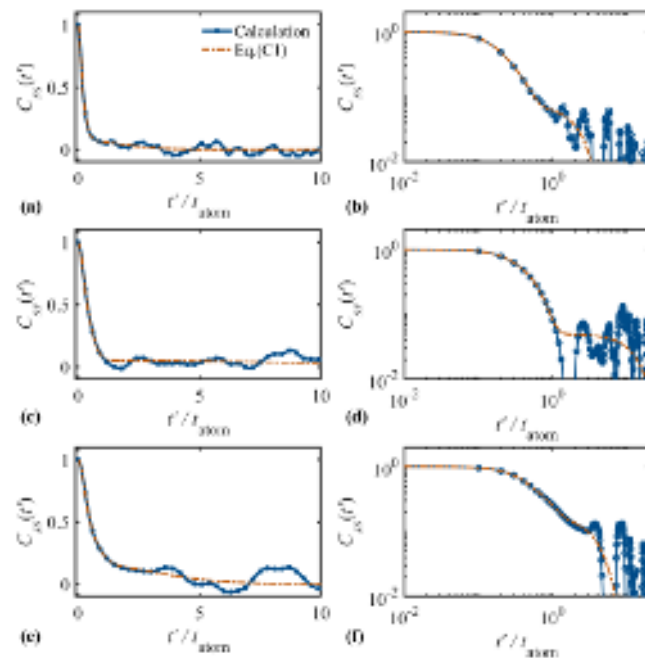


FIG. 24. Comparisons of the autocorrelation function of shear stresses, C_{ss} , for CG systems in the CG simulations with the fitting curves based on Eq.(E1) for different coarse-graining levels. (a) and (b): $n_{cg} = 4$, (c) and (d): $n_{cg} = 8$, (e) and (f): $n_{cg} = 12$.

REFERENCES

- ¹M. P. Allen and D. J. Tildesley, Computer simulation of liquids (Oxford university press, 2017).
- ²P. Hoogerbrugge and J. Koelman, “Simulating microscopic hydrodynamic phenomena with dissipative particle dynamics,” *Europhysics letters* **19**, 155 (1992).
- ³P. Español and P. Warren, “Statistical mechanics of dissipative particle dynamics,” *Europhysics letters* **30**, 191 (1995).
- ⁴R. Zwanzig, Nonequilibrium statistical mechanics (Oxford university press, 2001).
- ⁵M. G. Saunders and G. A. Voth, “Coarse-graining methods for computational biology,” *Annual Review of Biophysics* **42**, 73–93 (2013).
- ⁶P. Español and P. B. Warren, “Perspective: Dissipative particle dynamics,” *The Journal of Chemical Physics* **146** (2017), 10.1063/1.4979514.
- ⁷J. Jin, A. J. Pak, A. E. P. Durumeric, T. D. Loose, and G. A. Voth, “Bottom-up coarse-graining: Principles and perspectives,” *Journal of Chemical Theory and Computation* **18**, 5759–5791 (2022), doi: 10.1021/acs.jctc.2c00643.
- ⁸H. C. Andersen, “Molecular dynamics simulations at constant pressure and/or temperature,” *The Journal of Chemical Physics* **72**, 2384–2393 (1980).
- ⁹C. P. Lowe, “An alternative approach to dissipative particle dynamics,” *Europhysics Letters* **47**, 145 (1999).
- ¹⁰E. A. J. F. Peters, “Elimination of time step effects in dpd,” *Europhysics Letters* **66**, 311 (2004).
- ¹¹S. Nosé, “A molecular dynamics method for simulations in the canonical ensemble,” *Molecular Physics* **52**, 255–268 (1984), doi: 10.1080/00268978400101201.
- ¹²W. G. Hoover, A. J. C. Ladd, and B. Moran, “High-strain-rate plastic flow studied via nonequilibrium molecular dynamics,” *Physical Review Letters* **48**, 1818–1820 (1982), pRL.
- ¹³D. J. Evans and B. L. Holian, “The nose–hoover thermostat,” *The Journal of Chemical Physics* **83**, 4069–4074 (1985).
- ¹⁴G. J. Martyna, M. L. Klein, and M. Tuckerman, “Nosé–hoover chains: The canonical ensemble via continuous dynamics,” *The Journal of Chemical Physics* **97**, 2635–2643 (1992).
- ¹⁵H. J. C. Berendsen, J. P. M. Postma, W. F. van Gunsteren, A. DiNola, and J. R. Haak, “Molecular dynamics with coupling to an external bath,” *The Journal of Chemical Physics* **81**, 3684–3690 (1984).

- 751 ¹⁶C. Braga and K. P. Travis, “A configurational temperature nosé-hoover thermostat,” The Journal
752 of Chemical Physics **123** (2005), 10.1063/1.2013227.
- 753 ¹⁷M. P. Allen and F. Schmid, “A thermostat for molecular dynamics of complex fluids,” Molecular
754 Simulation **33**, 21–26 (2007).
- 755 ¹⁸S. Pieprzyk, D. M. Heyes, S. Maćkowiak, and A. C. Brańka, “Galilean-invariant nosé-hoover-
756 type thermostats,” Physical Review E **91**, 033312 (2015).
- 757 ¹⁹A. Kumar, Y. Asako, E. Abu-Nada, M. Krafczyk, and M. Faghri, “From dissipative particle
758 dynamics scales to physical scales: a coarse-graining study for water flow in microchannel,”
759 Microfluidics and Nanofluidics **7**, 467 (2009).
- 760 ²⁰Z. Li, Y.-H. Tang, H. Lei, B. Caswell, and G. E. Karniadakis, “Energy-conserving dissipative
761 particle dynamics with temperature-dependent properties,” Journal of Computational Physics
762 **265**, 113–127 (2014).
- 763 ²¹H. Lei, B. Caswell, and G. E. Karniadakis, “Direct construction of mesoscopic models from
764 microscopic simulations,” Physical Review E **81**, 026704 (2010).
- 765 ²²M. B. Liu, G. R. Liu, L. W. Zhou, and J. Z. Chang, “Dissipative particle dynamics (dpd): An
766 overview and recent developments,” Archives of Computational Methods in Engineering **22**,
767 529–556 (2015).
- 768 ²³T. Kinjo and S. Hyodo, “Equation of motion for coarse-grained simulation based on microscopic
769 description,” Physical Review E **75**, 051109 (2007).
- 770 ²⁴Y. Yoshimoto, I. Kinefuchi, T. Mima, A. Fukushima, T. Tokumasu, and S. Takagi, “Bottom-up
771 construction of interaction models of non-markovian dissipative particle dynamics,” Physical
772 Review E **88**, 043305 (2013).
- 773 ²⁵Y. Yoshimoto, Z. Li, I. Kinefuchi, and G. E. Karniadakis, “Construction of non-markovian
774 coarse-grained models employing the mori–zwanzig formalism and iterative boltzmann inver-
775 sion,” The Journal of Chemical Physics **147** (2017), 10.1063/1.5009041.
- 776 ²⁶Z. Li, H. S. Lee, E. Darve, and G. E. Karniadakis, “Computing the non-markovian coarse-
777 grained interactions derived from the mori-zwanzig formalism in molecular systems: Applica-
778 tion to polymer melts,” Journal of Chemical Physics **146**, 014104 (2017).
- 779 ²⁷G. Jung, M. Hanke, and F. Schmid, “Generalized langevin dynamics: construction and numeri-
780 cal integration of non-markovian particle-based models,” Soft Matter **14**, 9368–9382 (2018).
- 781 ²⁸T. Ye, B. Jing, and D. Pan, “Intelligent dissipative particle dynamics: Bridging mesoscopic mod-
782 els from microscopic simulations via deep neural networks,” Journal of Computational Physics

783 **475**, 111857 (2023).

784 ²⁹P. E. Kloeden and E. Platen, Numerical Solution of Stochastic Differential Equations (Springer,
785 Berlin, Heidelberg, 1992).

786 ³⁰B. Leimkuhler and C. Matthews, “Rational construction of stochastic numerical methods for
787 molecular sampling,” *Applied Mathematics Research eXpress* **2013**, 34–56 (2012).

788 ³¹B. Leimkuhler and C. Matthews, “Robust and efficient configurational molecular sampling via
789 langevin dynamics,” *The Journal of Chemical Physics* **138** (2013), 10.1063/1.4802990.

790 ³²H. C. Andersen, “Rattle: A “ velocity ” version of the shake algorithm for molecular dynamics
791 calculations,” *Journal of Computational Physics* **52**, 24–34 (1983).

792 ³³L. V. Woodcock, “Isothermal molecular dynamics calculations for liquid salts,” *Chemical
793 Physics Letters* **10**, 257–261 (1971).

794 ³⁴W. C. Swope, H. C. Andersen, P. H. Berens, and K. R. Wilson, “A computer simulation method
795 for the calculation of equilibrium constants for the formation of physical clusters of molecules:
796 Application to small water clusters,” *The Journal of Chemical Physics* **76**, 637–649 (1982).

797 ³⁵J. G. Greener, “Differentiable simulation to develop molecular dynamics force fields for disor-
798 dered proteins,” *Chemical Science* **15**, 4897–4909 (2024).

799 ³⁶D. C. Rapaport, The art of molecular dynamics simulation (Cambridge university press, 1995).

800 ³⁷M. Tuckerman, B. J. Berne, and G. J. Martyna, “Reversible multiple time scale molecular
801 dynamics,” *The Journal of Chemical Physics* **97**, 1990–2001 (1992).

802 ³⁸H. Wang, C. Junghans, and K. Kremer, “Comparative atomistic and coarse-grained study of
803 water: What do we lose by coarse-graining?” *European Physical Journal E* **28**, 221–229 (2009).

804 ³⁹M. Guenza, “Thermodynamic consistency and other challenges in coarse-graining models,” *Eu-
805 ropean Physical Journal-Special Topics* **224**, 2177–2191 (2015).